Electronic Theses and Dissertations

Theses, Dissertations, and Major Papers

11-8-2023

Enhanced Mathematical Modeling and Novel Multiparameter Estimation Scheme for PMSMs Accounting for Nonlinearities

Sana Etemadi
University of Windsor

Enhanced Mathematical Modeling and Novel Multiparameter Estimation Scheme for PMSMs Accounting for Nonlinearities

By

Sana Etemadi

A Thesis
Submitted to the Faculty of Graduate Studies
through the Department of Electrical & Computer Engineering
in Partial Fulfillment of the Requirements for
the Degree of Master of Applied Science
at the University of Windsor

Windsor, Ontario, Canada

Enhanced Mathematical Modeling and Novel Multiparameter Estimation Scheme for PMSMs Accounting for Nonlinearities

by

Sana Etemadi

APPROVED BY:

_____
O. A. Jianu
Department of Mechanical, Automotive & Materials Engineering

_____
B. Balasingam
Department of Electrical & Computer Engineering

_____
N. C. Kar, Advisor
Department of Electrical & Computer Engineering

October 16, 2023

DECLARATION OF CO-AUTHORSHIP/PREVIOUS PUBLICATIONS

I.   Co-Authorship

I hereby declare that this thesis incorporates material that is the result of joint research, as follows:

This thesis includes the outcome of publication which also has co-authors who are/were graduate students or post-doctoral fellows supervised by Dr. Narayan Kar. In all cases, only the primary contributions of the author towards these publications are included in this thesis. The contribution of co–authors was primarily through the provision of assistance in experimentation and analysis.

I am aware of the University of Windsor Senate Policy on Authorship, and I certify that I have properly acknowledged the contribution of other researchers on my thesis and have obtained written permission from each of the co–authors to include the above material(s) in my thesis. I certify that, with the above qualification, this thesis, and the research to which it refers, is the product of my own work.

II.   Previous Publication

This thesis includes selected sections and extended work of research that have been published/submitted for publication in peer-reviewed IEEE International Conferences, as follows:

Thesis Chapter	Publication title/Full citation	Publication status
2, 3	**S. Etemadi,** H. Cheng, M. S. Toulabi, U. Deshpande and N. C. Kar, "Multiparameter Estimation Accuracy Improvement for PMSMs Using a Constriction Coefficient-Based Particle Swarm Optimization," 2023 *IEEE* 32*nd International Symposium on Industrial Electronics (ISIE)*, Helsinki, Finland, 2023, pp. 1-6, doi: 10.1109/ISIE51358.2023.10227963.	*Published*

I certify that I have obtained written permission from the copyright owners to include the above published materials in my thesis. I certify that the above material describes work completed during my registration as a graduate student at the University of Windsor.

III.   General

I declare that, to the best of my knowledge, my thesis does not infringe upon anyone's copyright nor violate any proprietary rights and that any ideas, techniques, quotations, or any other material from the work of other people included in my thesis, published or otherwise, are fully acknowledged in accordance with the standard referencing practices. Furthermore, to the extent that I have included copyrighted material that surpasses the bounds of fair dealing within the meaning of the Canada Copyright Act and has included copies of such copyright clearances to the appendix of this thesis.

I declare that this is a true copy of my thesis, including any final revisions, as approved by my thesis committee and the Graduate Studies office, and that this thesis has not been submitted for a higher degree to any other University or Institution.

ABSTRACT

PMSMs are widely used in various industrial applications, including EVs, due to their high power density, high efficiency, and precise control characteristics. Accurate parameter identification is crucial for optimal controller design, fault detection, performance optimization, and condition monitoring in PMSMs. This thesis investigates advanced parameter estimation techniques for PMSMs to enhance the accuracy and reliability of the estimation process. A novel noninvasive multiparameter estimation approach is proposed to estimate the electrical parameters of PMSM, including the stator winding resistance, PM flux linkage, and dq-axis inductances. The method incorporates compensation techniques to address VSI nonlinearity and the magnetic saturation effect is modeled through polynomial functions, and the effect of temperature on the stator winding resistance is compensated. A method for decoupling the parameters in the PMSM dq-axis voltage equations is proposed to reduce both the computational burden and cross-coupling effects between parameters. Three objective functions are defined and implemented using the CCPSO algorithm which improves the estimation accuracy and efficiency. Experimental validation is carried out on a 4.25-kW interior PMSM under varying speed and load conditions, and error analysis is performed that compares the estimated and measured parameters, demonstrating high accuracy. A comparative analysis is also conducted with the least squares algorithm, which indicates better estimation results for CCPSO.

A parameter-independent model for MTPA control of PMSMs is proposed, eliminating the need for online parameter estimation, and increasing computational efficiency. A gradient descent algorithm-based current angle search approach is also proposed and validated through simulations. This thesis includes parameter sensitivity analysis to enhance parameter reliability. The Taguchi method, a reliable and efficient experimental design technique, is implemented to investigate the sensitivity of PMSM parameters to key factors like torque, speed, and temperature at different levels.

Dedicated to my mother and my sister,

I love you …

In honor of all the courageous Iranian women who continue to shine brightly, showing the world their resilience and grace.

ACKNOWLEDGEMENTS

TABLE OF CONTENTS

LIST OF TABLES

LIST OF FIGURES

LIST OF ABBREVIATIONS/SYMBOLS

Abbreviation	Explanation
AC	Alternating Current
ABS	Artificial Bee Colony Algorithms
ACO	Ant Colony Optimization
AGA	Adaptive Genetic Algorithm
AI	Artificial Intelligence
ANN	Adaline Neural Network
AO	Adaptive Observer
APA	Affine Projection Algorithm
APSO	Adaptive PSO
BBC	Biogeography-Based Optimization
BEV	Battery Electric Vehicle
BFGS	Broyden Fletcher Goldfarb Shanno
BLDC	Brushless DC Motor
CCPSO	Constriction Coefficient-based PSO
CCS	Cuckoo Search Algorithm
CFO	Chaotic Firefly Optimization
DC	Direct Current
DE	Differential Evolution
DO	Disturbance Observer
DOE	Design of Experiment
DTC	Direct Torque Control
DWPSO	Decreasing Weight PSO
EA	Evolutionary Algorithm
EKF	Extended Kalman Filter
EMF	Electromotive Force
ES	Evolutionary Strategies
EV/ HEV	Electric/Hybrid Vehicle
ER-EV	Extended-Range Electric Vehicle

FCEV	Fuel Cell Electric Vehicle
FEA	Finite Element Analysis
FFT	Fast Fourier Transform
FOC	Field-Oriented Control
FPGA	Field-Programmable Gate Array
GA	Genetic Algorithm
GD	Gradient Descent
GP	Genetic Programming
GSA	Gravitational Search Algorithm
GWO	Grey Wolf Optimizer
HF	High Frequency
ICE	Internal Combustion Engine
IGBT	Insulated-Gate Bipolar Transistor
IM	Induction Motor
IPMSM	Interior Permanent Magnet Synchronous Motor
IPSO	Improved PSO
ITSC	Inter-Turn Short Circuit
LCR	Inductance, Capacitance, and Resistance
LS	Least Square
MPC	Model Predictive Control
MRAS	Model Reference Adaptive System
MTPA	Maximum Torque Per Ampere
MTPV	Maximum Torque Per Voltage
NN	Neural Network
OF	Objective Function
OFAT	One-Factor-At-Time
PHEV	Plug-in Hybrid Electric Vehicle
PI	Proportional Integral
PLC	Programmable Logic Controller
PMSM	Permanent Magnet Synchronous Motor
PM	Permanent Magnet

PMM	Permanent Magnet Motor
POPE	Position-Offset based Parameter Estimation
PSO	Particle Swarm Optimization
PWM	Pulse Width Modulation
RLS	Recursive Least Square
SFR	Standstill Frequency Response
SGA	Standard Genetic Algorithm
SMO	Sliding Mode Observer
SNR	Signal-to-Noise Ratio
SoH	State of Health
SPMSM	Surface Mounted PMSM
SPSO	Standard PSO
SQP	Sequential Quadratic Programming
SRM	Switched Reluctance Motor
RTS	Real-Time Simulator
THD	Total Harmonic Distortion
TVPSO	Time-Varying PSO
VC	Vector Control
VSD	Vector Space Decomposition
VSI	Voltage Source Inverter

NOMENCLATURE

c_1, c_2	Acceleration coefficients of PSO
D_d, D_q	Distorted coefficients of VSI's dead time voltage
D_D, D_Q	Average values of the distorted coefficients in one electrical cycle
G_{best}	The best position found by the entire swarm
$G_j(t)$	j^{th} component of the global best position
i_d, i_q, i_s	dq-axis currents and stator current [A]
I_d, I_q	Average values of dq-axis currents [A]
I_s	Stator phase current [A]
L_d, L_q	dq-axis inductances [H]
L_{d0}, L_{q0}	Unsaturated dq-axis inductances [H]
$\hat{L}_d, \hat{L}_q$	Estimated dq-axis inductances [H]
$\hat{L}_{d0}, \hat{L}_{q0}$	Estimated unsaturated L_d and L_q [H]
$\hat{L}_{d,i}, \hat{L}_{q,i}$	Estimated L_d and L_q at i^{th} population [H]
P_{best}	The best position found by each particle
$P_{ij}(t)$	j^{th} component of the personal best position of the ith particle
R_s	Stator's phase winding resistance [Ω]
$\hat{R}_{s,i}$	Estimated resistance at i^{th} population [Ω]
r_1, r_2	Random numbers in a range of [0, 1]
u_d, u_q	dq-axis actual voltages [V]
v_d, v_q, v_s	Reference voltages from the output of the PI controllers and reference stator voltage [V]
V_d, V_q	Average values of reference voltages [V]
V_{dead}	Distorted voltage of VSI nonlinearity [V]
$\hat{V}_{dead,i}$	Estimated V_{dead} at i^{th} population [V]
$V_{ij}(t)$	j^{th} component of the current velocity vector of the ith particle
$V_{ij}(t+1)$	j^{th} component of the updated velocity

$X_{ij}(t)$	j^{th} component of the current position vector of the ith particle
$X_{ij}(t+1)$	j^{th} component of the updated position vector of the ith particle
α_1 to α_5	Saturation coefficients defined in L_d polynomial function
$\hat{\alpha}_1$ to $\hat{\alpha}_5$	Estimated L_d saturation coefficients
$\hat{\alpha}_{1,i}$ to $\hat{\alpha}_{5,i}$	Estimated L_d saturation coefficients at i^{th} population
β_1 to β_5	Saturation coefficients defined in L_q polynomial function
$\hat{\beta}_1$ to $\hat{\beta}_5$	Estimated L_q saturation coefficients
$\hat{\beta}_{1,i}$ to $\hat{\beta}_{5,i}$	Estimated L_q saturation coefficients at i^{th} population
$\varphi, \varphi_1, \varphi_2, \chi$	Constriction factors
γ	Current angle, the angle between the stator current vector and positive q-axis [deg]
δ	Voltage angle, the angle between the stator voltage vector and positive q-axis [deg]
θ	Rotor position [deg]
λ_{PM}	Permanent magnet flux linkage [Wb.Turn]
$\hat{\lambda}_{PM,i}$	Estimated λ_{PM} at i^{th} population [Wb.Turn]
τ_{e_cal}	Calculated electromagnetic torque [Nm]
τ_m	Magnetic torque [Nm]
τ_{meas}	Measured torque of torque transducer [Nm]
τ_r	Reluctance torque [Nm]

CHAPTER 1

Introduction

The increasing demand for sustainable transportation has propelled the rapid expansion and advancement of electric vehicles (EVs), highlighting the industry's commitment to greener and more environmentally friendly solutions. This chapter provides an overview of EVs and their global market. It encompasses a literature review on traction motors used in EVs, specifically permanent magnet synchronous motors. In addition, advanced electric motor parameter estimation techniques and their associated challenges are discussed.

This chapter is structured as follows: Section 1.1 analyzes the current trends and developments in EVs and the market dynamics driving the widespread adoption of EVs and their potential impact on sustainable transportation. Section 1.2 provides insights into various traction motor and drive technologies employed in EVs, highlighting their features, advantages, and challenges. A comprehensive literature survey is conducted on state-of-the-art parameter estimation techniques in Section 1.3, to explore the latest methodologies for estimating and optimizing system parameters to enhance EV performance. In Section 1.4, the difficulties associated with parameter estimation and the practical challenges encountered while implementing parameter estimation techniques are discussed. Sections 1.5 and 1.6 outline the research objectives and contributions, clearly defining the aims and expected outcomes of the thesis. Section 1.7 provides an overview of the organization of the thesis. Finally, Section 1.8 concludes the chapter with a list of references.

1.1. Overview of Electric Vehicle Technology

Electric vehicles utilize electricity as a source of energy instead of relying on gasoline or diesel. This alternative form of transportation brings forth a multitude of advantages when compared to internal combustion engine (ICE) vehicles. One prime benefit lies in their ability to emit significantly lower levels of greenhouse gases and carbon dioxide, which plays a pivotal role in mitigating the issue of climate change. Moreover, this transition to EVs also helps diminish our dependence on finite fossil fuels and move towards a more sustainable future [1], [2].

The global market for EVs has rapidly increased over the last decade. Compelling interest in electrification has propelled automakers worldwide to increase their manufacturing of EVs, which has led to a growth in sales.

In 2022 the global sales of EVs comprising both battery electric vehicles (BEVs) and plug-in hybrid electric vehicles (PHEVs), reached a total of 10.5 million units marking a significant increase of 55% compared to the previous year, as shown in Fig. 1.1 [3]. Meanwhile, the combined sales of BEVs and PHEVs accounted for approximately 13% of all global light-vehicle sales in 2022. It is projected that EV sales will continue to rise, and an estimated total of 14.3 million EVs will be sold by the end of 2023. This represents a growth rate of 36% compared with the previous year [3].
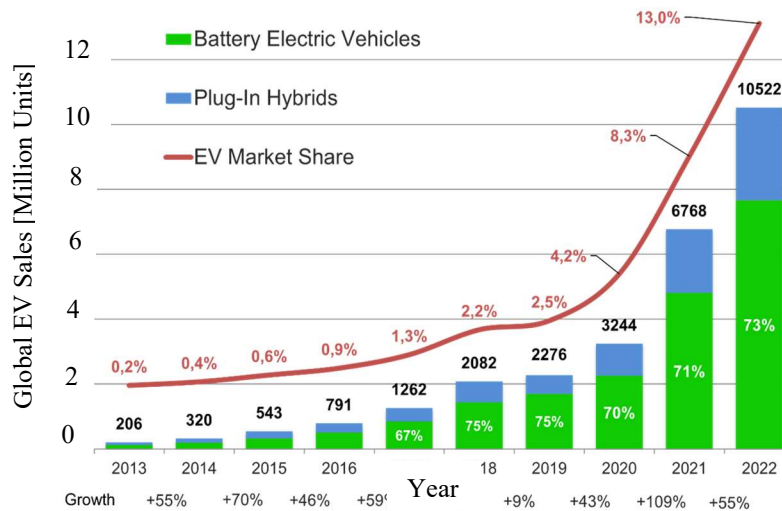
Fig. 1.1. Global electric vehicle sales (BEV & PHEV) [3].

Advance in engine technology and shifting market demands have led to the development of different types of EVs, including BEVs, PHEVs, hybrid electric vehicles (HEVs), fuel cell EVs (FCEVs), and extended-range EVs (ER-EVs) [4].

Figure 1.2 [5] illustrates the physical powertrain layout of an all-wheel-drive BEV Mercedes-Benz SLS AMG E-Cell model, which consists of multiple electric motors and a large battery pack, providing all-electric propulsion and zero emissions.
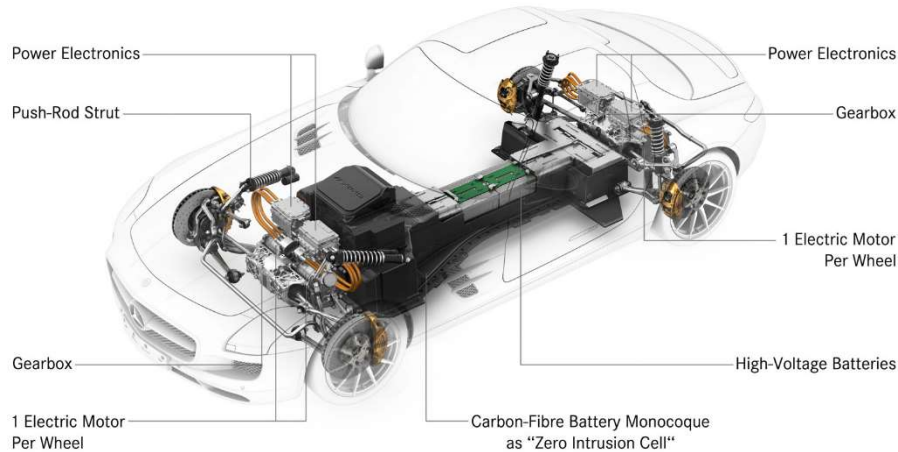
Fig. 1.2. Powertrain layout of Mercedes-Benz SLS AMG E-Cell [5].

1.2. Review of Traction Motors in EVs

EVs comprise a variety of components, including rechargeable batteries, onboard chargers, power electronics (such as DC/DC converters and inverters), thermal management systems, transmissions, differentials, gearboxes, and traction motors. The key components crucial for EV operation are the battery pack, inverter, and traction motor. At the core of an EV, a traction motor converts electrical energy into mechanical power to propel the vehicle. It plays a vital role in delivering efficient and powerful performance, enabling smooth acceleration and responsive control. The efficiency and performance of a traction motor have a direct impact on the range, acceleration, and overall capabilities of electric vehicles. There are several candidates for traction motors used in EV/HEVs, such as permanent magnet synchronous motors, induction motors (IMs), switched reluctance motors (SRMs), and brushless DC motors (BLDC), each of which has its own set of advantages and disadvantages. Figure 1.3 depicts the various electric motor types that are available for EV/HEVs [6].

PMSMs have garnered significant research attention in recent years owing to their benefits, such as high power density, high torque, and efficiency, as well as efficient operation across a wide torque-speed range and precise control characteristics. The presence of embedded magnets in the rotor to generate the magnetic field eliminates the need for field windings, resulting in a compact and lightweight motor that reduces losses and improves efficiency. By contrast, IMs and SRMs do not utilize magnets and are known

for their robustness and cost-effectiveness. A suitable cooling topology is required for IMs to dissipate the heat generated on both the stator and rotor sides. The exceptional robustness of SRMs, making them suitable for harsh environments and fault-tolerant operations. However, their drawback is the generation of high levels of acoustic noise and vibrations during operation. Table 1.1 listed a comparison of the widely utilized traction motors for EV applications [7].
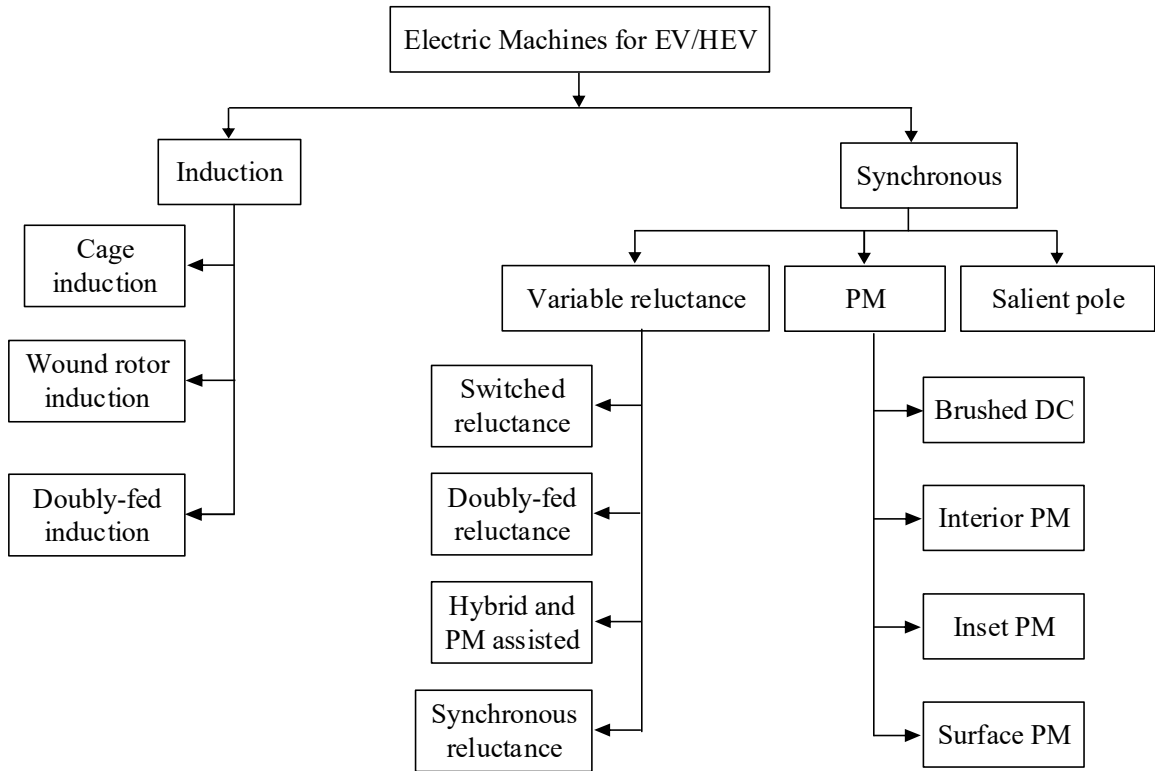
Fig. 1.3. Available electric motor types for EV/HEVs [6].

TABLE 1.1
COMPARISON OF TRACTION MOTORS IN EV APPLICATIONS

Traction Motor	Rotor Design	Stator Design	Power Density	Efficiency	Size	Cost	Noise & Vibration
PMSM	Permanent Magnet	Wound Stator	High	High	compact	High	Low
Induction	Squirrel Cage or Wound Rotor	Wound Stator	Medium	Medium	Medium	Medium	Medium
SRM	Salient Pole	Wound Stator	High	High	Large	Low	High
BLDC	Permanent Magnet	Wound Stator	High	High	compact	High	Low

1.3. Parameter Estimation of PMSMs: Significance and Associated Challenges

PMSMs are preferred over other types of electric motors in EV/HEVs owing to their advantages of high power and torque densities, high efficiency, and low torque ripples. Due to the nonlinear behavior of the machine, the electrical and mechanical parameters are subject to variations under different operating conditions. Various factors incorporating mechanical vibration, thermal properties, and loading conditions have noticeable effects on the PMSM's electrical and mechanical characteristics. Therefore, accurate estimation of PMSM parameters is crucial for optimal controller design, fault detection and diagnosis, condition monitoring, and motor performance optimization. Additionally, in EV/HEV applications, accurate knowledge of electrical parameters is crucial to determine the optimal current trajectories under maximum torque per ampere (MTPA) and maximum torque per voltage (MTPV) control strategies. In commonly employed control methodologies for PMSMs, such as field-oriented control (FOC), direct torque control (DTC), and model predictive control (MPC), precise PMSM parameters are usually essential for guaranteeing system stability, improving efficiency, and dynamic system response [8].

There are several challenges associated with the parameter estimation of PMSMs, and Fig. 1.4 summarizes some of them. A full estimation of electrical and mechanical parameters requires a full-rank model. However, as shown in (1.1), the rank of the PMSM electrical equations in the direct and quadrature (dq) reference frames is two, which means that only two parameters can be estimated simultaneously using these equations, whereas four unknown electrical parameters, including the stator winding resistance, permanent magnet flux linkage, d- and q-axis inductances, need to be estimated. This is called rank deficiency when the number of unknown parameters is greater than the number of equations. Consequently, the parameters estimated from the rank-deficient model may converge to incorrect values. To mitigate this problem, various techniques have been proposed using online and offline estimation methods, which are discussed in the next section. For instance, a disturbance DC/AC signal, such as a voltage/current, can be injected into the machine to generate more sets of equations and solve the rank-deficient problem [9], [10].

$$u_d = R_s i_d + L_d \frac{di_d}{dt} - \omega_e L_q i_q$$

$$u_q = R_s i_q + L_q \frac{di_q}{dt} + \omega_e L_d i_d + \omega_e \lambda_{PM}$$

(1.1)
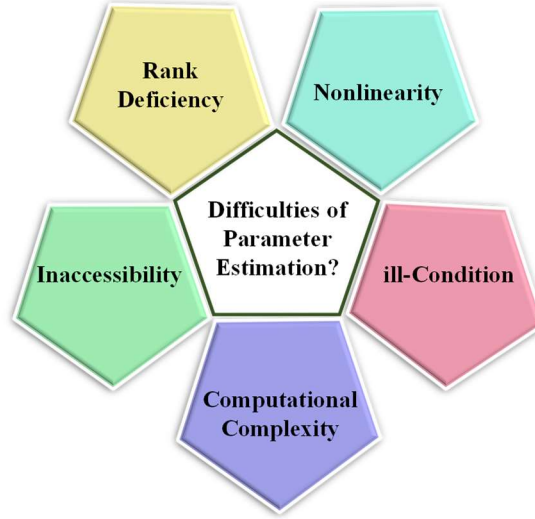
Fig. 1.4. Difficulties and challenges in parameter estimation of PMSMs.

Due to magnetic saturation, iron core loss, and non-sinusoidal back electromotive force (EMF), PMSMs exhibit nonlinear behavior that varies with operating conditions, including temperature, load, and speed variations. In a pulse-width-modulated (PWM)-fed voltage source inverter (VSI), there is a non-ideal voltage gain between the reference and actual terminal voltages of the PMSM that is caused by blanking time, DC bus voltage error between the measured and real DC voltage, and nonideal inherent characteristics of power switches such as voltage drops, turn on/off time, and output voltage transition time [10], [11]. Additionally, at high torque levels, PMSMs experience magnetic saturation, leading to deviations in motor performance and affecting the accuracy of the parameter estimation. Due to the imperfect construction symmetry of the machine, cross-coupling effects exist and have a significant impact on the magnetic behavior and variation of the equivalent circuit parameters of the PMSM. The *dq*-axis flux linkages are functions of the *dq*-axis currents, and for accurate parameter estimation, nonlinearity arising from cross-coupling and magnetic saturation effects must be taken into account [12]–[14]. These nonlinearities cause current distortions, torque ripples, and degradation of machine control performance. Typically, they are more severe in high-speed regions than in low-speed regions.

6

Parameter estimation performance in the PMSM model can be adversely affected by model uncertainties and measurement noise. These factors may lead to decreased process reproducibility, a condition known as an "ill-condition" in mathematical terms. An ill-conditioned problem indicates that the estimated parameters become highly sensitive to perturbations in the input and output data, which are primarily caused by sensor noise and computational processes [9]. Many parameter estimation techniques involve solving nonlinear optimization problems and minimizing the error between the measured data and model predictions. Advanced optimization algorithms, particularly artificial intelligence-based techniques, can be computationally intensive and time-consuming. Balancing the trade-off between estimation accuracy and computation time is challenging and important. Additionally, in real-time applications, multiple parameters may need to be estimated simultaneously, and they have coupling effects that make the estimation process more complex. As the computing capabilities of processors have undergone substantial advancements over the years, computational processes have become less complex and require shorter execution times. During motor operation and in some hazardous environments, or when the motor is sealed or embedded it is physically challenging to access the motor and connecting sensors for measurements.

The challenge of inaccessibility arises in motor parameter estimation when the motor is operating in hazardous environments or when it is sealed or embedded within machinery, making it difficult to access the motor and connect sensors for data measurement. This limitation can prevent the direct acquisition of critical data required for accurate parameter estimation, leading to the need for alternative methods to estimate motor parameters effectively.

1.4. Review of State-of-the-Art Parameter Estimation Techniques for PMSMs

Several techniques have been developed for PMSM's parameter estimation over the last few decades. Based on the operating conditions of the machine, these techniques are often classified as online and offline methods. Offline estimation is typically performed prior to or after the motor operation, frequently by disconnecting the motor from the load or at a standstill condition. This involves utilizing the input/output data and estimating the PMSM parameters afterward by post-processing the collected data. Online estimation is

conducted during motor operation, with its load connected and continuously obtaining new measured input/output data and updating the electrical parameter values in real-time operation [8]. The offline parameter estimation methods are comprehensively discussed in [8] encompassing the time and frequency domain-based methods and finite element analysis (FEA). Online parameter estimation techniques are well reviewed in [9]. Figure 1.5 categorizes the online and offline parameter estimation techniques for PMSMs [8], [9]. Commonly employed computational methods for PMSM parameter estimation include numerical, observer-based, and artificial-intelligence-based methods, as illustrated in Fig. 1.6 [8].
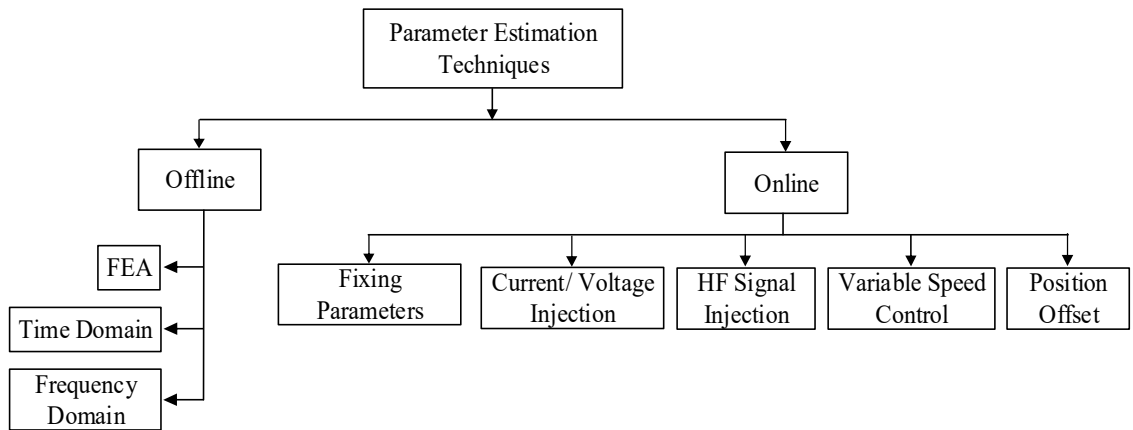
Fig. 1.5. The classification of existing PMSM parameter estimation techniques [8], [9].
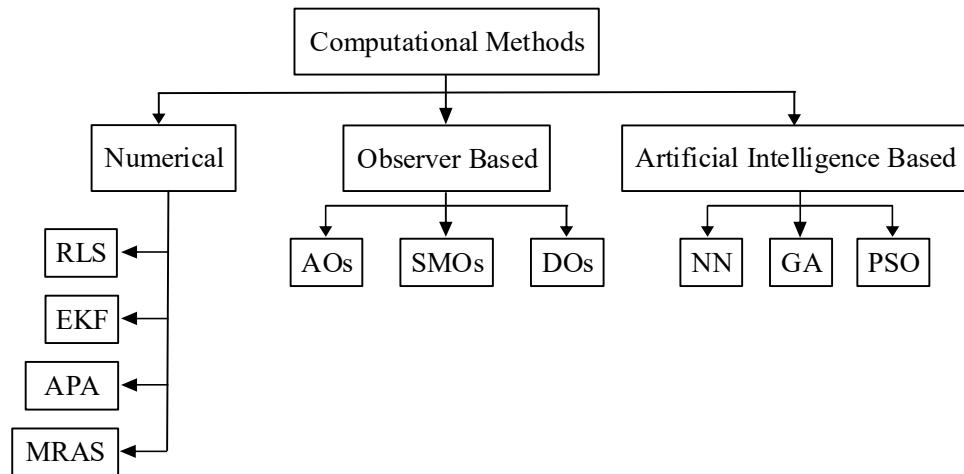
Fig. 1.6. Most common computational methods for PMSM parameter estimation [8].

Among offline methods, frequency-domain-based methods primarily employ standstill frequency response (SFR) tests, which are mainly categorized into power amplifier-driven SFR and VSI-driven SFR. These tests measure the responses to predefined deterministic

or periodic excitation signals and extract the *dq*-axis equivalent parameters from the collected data. The power amplifier-driven SFR uses a high-power linear amplifier to generate waveforms, whereas the VSI-driven SFR test utilizes VSIs as waveform generators and considers factors such as accuracy, measurement time, and sensitivity to noise when selecting excitation signals, and has the advantage of advancement in VSIs to generate excitation signals. The recommended frequency range for conducting SFR tests is 0.001–1 kHz; however, higher frequencies can also be applied. Offline time-domain parameter estimation techniques use time-domain responses to impose perturbations or excitation signals. These methods are performed under specific laboratory conditions and encompass a search coil, load, phase voltage measurement, AC standstill, locked rotor, DC-biased AC signal injection, and torque tests. The search coil test uses fixed stator coils to determine the flux of the PMSM. The load test provided accurate torque-angle measurements for better parameter identification. The phase voltage measurement test determines the *dq*-axis inductances using an additional synchronous machine setup. The AC standstill test measures the self-and mutual inductances to calculate the *dq*-axis inductances. The vector current-controlled test identifies the *dq*-axis inductances without the need for additional equipment. The locked-rotor test uses a VSI to determine current-dependent flux linkage. The DC-biased AC signal injection test estimates the *dq*-axis inductances with the DC bias and AC signals. The torque test estimates the torque constant and *dq*-axis inductances using a DC supply and a torque sensor [7], [8]. FEA is the most common offline method and is a powerful simulation tool that uses mathematical modeling and serves multiple purposes. It aids motor designers in designing the motor, provides an in-depth analysis of its behavior, and facilitates the determination of the motor parameters under various operating conditions. However, FEA requires detailed and accurate knowledge of the structure, geometry, material, and design of PMSM for successful calculation and parameter identification.

The simplest technique for parameter estimation is multistep estimation, which involves fixing one or more motor parameters to their nominal values. However, the estimation error in this method is remarkable since the parameters may vary due to magnetic saturation, temperature, cross-coupling effects, and other machine nonlinearities. Many online parameter estimation techniques involve the injection of a disturbance signal

into the machine at a standstill or during motor operation to generate extra PMSM steady-state electrical equations and solve the rank deficiency issue. Additional AC/DC signals such as voltage, current, position offsets, or high-frequency (HF) signals can be injected into the drive system. Among them, current injection is the most common method since it is capable of estimating all electrical parameters including stator resistance, dq-axis inductances, and PM flux linkage, and has been widely investigated in [15]–[22]. In [16] and [17], first steady-state measurements were collected during IPMSM operation, thereafter, two small negative d-axis currents were orderly injected into the drive system for a very short time to obtain two additional sets of IPMSM electrical equations in steady-state and create a full-rank model, as illustrated in Fig. 1.7 and Fig. 1.8. After collecting all measurements in a steady state, electrical parameters, including stator winding resistance, PM flux linkage, and dq-axis inductances, were estimated using the recursive least square (RLS) algorithm considering magnetic saturation and using a linear equation to model the self- and cross-saturation of the dq-axis inductance during the current injection.

In [17], the vector space decomposition (VSD)-based model for a dual three-phase IPMSM was established, magnetic saturation and temperature effects were considered, the voltage source inverter measurement error is compensated in the mathematical models, and all electrical parameters were estimated using an improved RLS. The PM and stator winding temperatures were simultaneously estimated in [18] by employing the current injection approach using the Kalman filter (KF) for estimation with inductance cancellation and eliminating the VSI nonlinearity effect. To improve the accuracy of PMSM parameter estimation using the current injection-based methods, [19] investigated the influence of the amplitude and duration of the injected current under different machine operating conditions, such as torque loads, speeds, and temperatures, in order to select the appropriate conditions. Signal injection-based parameter estimation methods are referred to as invasive methods because they may introduce torque ripples, harmonics, and distortions in the PMSM, which degrade the drive system performance. In [16], a compensation strategy was proposed by injecting a q-axis current to minimize the torque ripples caused by the d-axis current injection. The techniques that require the injection of perturbations into the machine are invasive whereas the methods not introducing any disturbance and using the sensor measurements or simulation-based techniques are referred as noninvasive methods.
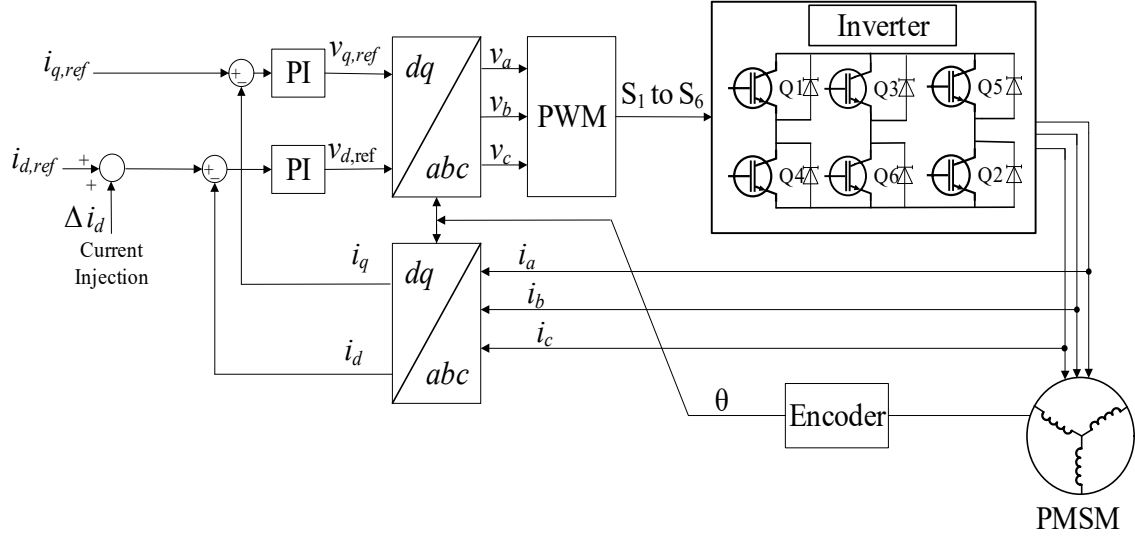
Fig. 1.7. Control schematic of the current injection strategy for PMSM parameter estimation.
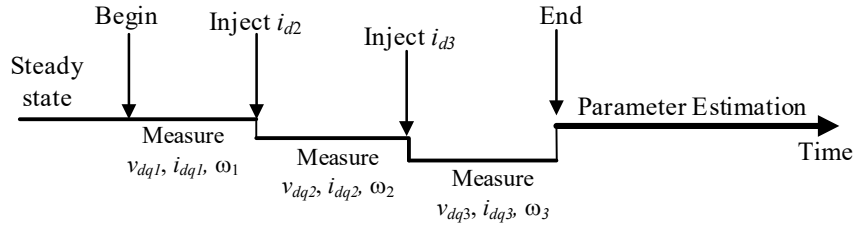
Fig. 1.8. Current injection strategy employed in [15] and [16].

Position offset-based parameter estimation (POPE) is also a widely known online parameter estimation technique for PMSMs employed in [23]–[25]. In [23], under a field-oriented variable-speed control system, two sets of PMSM data, namely, Data 1 and Data 2, were measured after the addition of positive and negative position offsets ($\Delta\theta_p$, $\Delta\theta_n$), as demonstrated in Figs. 1.9 and 1.10, and the PM flux linkage was estimated. The winding resistance and q-axis inductance were estimated using data without the addition of position offsets. However, this method is applied under the $i_d = 0$ control, so it fails to estimate d-axis inductance and it is not suitable to be applied for applications involving flux weakening control and under the high-performance operation of PMSM. Since the currents are set to constant values and not varying, the estimation of the PM flux linkage is not affected by VSI nonlinearity.

11
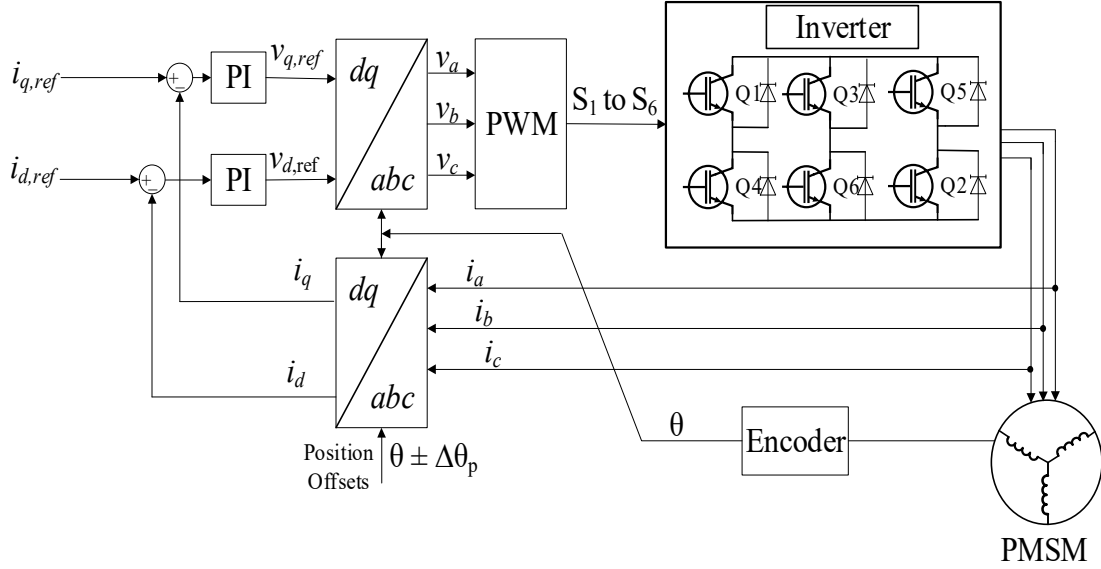
Fig. 1.9. Control schematic of the position offset-based strategy for PMSM parameter estimation.
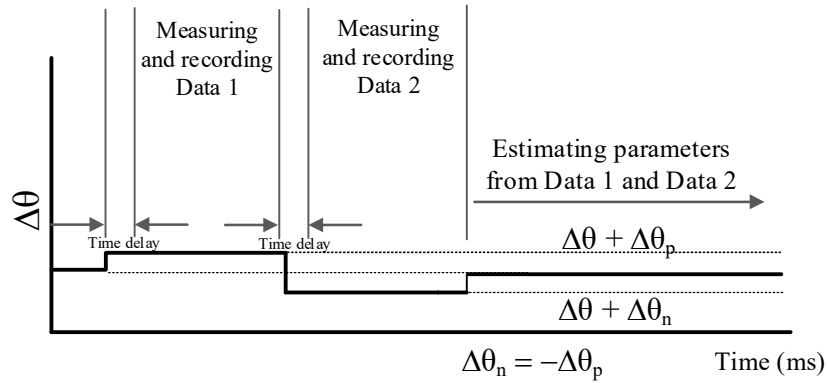
Fig. 1.10. Position offset addition strategy utilized in [23] and [24].

1.5. Thesis Research Objectives

Accurate knowledge of the PMSM parameters is essential for achieving high-performance control and optimizing its efficiency. The nonlinear characteristics of a machine result in discrepancies between nominal parameters and their actual values. Additionally, manufacturers often do not disclose detailed information about machine parameters. This lack of information can be challenging for engineers and researchers since accurate parameters are required for designing controllers, fault detection and diagnosis, performance optimization, and condition monitoring. This research aims to introduce a novel noninvasive scheme for the multiparameter estimation of PMSMs that considers machine nonlinearities. The objective is to improve the accuracy and efficiency of the

12

estimation process while achieving the overall goal of enhancing the performance of PMSMs. The objectives of this study are outlined below:

1. Develop a noninvasive PMSM multiparameter estimation scheme that accurately estimates all electrical parameters, including the stator winding resistance, PM flux linkage, and *dq*-axis inductances. Validation of the accuracy of the proposed parameter estimation scheme through experiments and analysis of collected data.

2. Investigate PMSM's nonlinear behavior and parameter variations of PMSMs under different operating conditions and incorporate machine nonlinearities in mathematical models to improve the accuracy of parameter estimation.

3. Analyze magnetic saturation effects and assess self- and cross-saturation impacts on the *dq*-axis inductances through accurate mathematical modeling.

4. Investigate the nonlinearity introduced by PWM-fed voltage source inverters and integrate it into a mathematical model to accurately update the reference voltages from the PI controllers to match the actual terminal voltages.

5. Developing the parameter-independent MTPA control-based torque equations and optimal current angle search method for MTPA control of PMSMs to maximize the torque and enhance motor efficiency.

6. Design of experiment using the Taguchi method to improve the efficiency and robustness of the experiment. Conduct a sensitivity analysis of the PMSM parameters to understand the effects of torque, speed, and temperature on the parameters by experimental validation.

1.6. Thesis Research Contributions

This thesis proposes a novel noninvasive approach for the multiparameter estimation of PMSMs with ease of implementation and accounting for motor nonlinearities, resulting in improved accuracy and efficiency of parameter estimation. The main contributions of the thesis are as follows:

➢ Improved accuracy of parameter estimation by incorporating magnetic saturation effects, self and cross-coupling effects, VSI nonlinearity, and temperature effects in the PMSM mathematical model for multiparameter estimation.

- ➢ Implemented decoupled scheme for decoupling multi-parameters to mitigate cross-coupling effects between parameters, resulting in enhanced efficiency and accuracy of estimation.
- ➢ Developed new cost functions within optimization algorithms leading to improved accuracy and efficiency of parameter estimation.
- ➢ Implementation, evaluation, and comparative analysis of multiple optimization and estimation algorithms in order to achieve higher accuracy and convergence speed.
- ➢ Validation of the proposed parameter estimation scheme through experimentation and analysis of collected data and performing error analysis to ensure its accuracy and reliability.
- ➢ Integration of MTPA control and multiparameter estimation for maximizing torque and improving motor efficiency.
- ➢ Investigating the sensitivity of parameters with improved experimental design using Taguchi method.

1.7. Organization of the Thesis

This thesis comprises 6 chapters, including the introductory chapter, that outlines the literature review, research work, and contributions aligned with the overall research objectives. The thesis is organized as follows:

Chapter 2 presents a mathematical model for a three-phase IPMSM that considers nonlinearities, including the effect of PWM-fed VSI and magnetic saturation. The Clarke-Park transformation is used to simplify the control and analysis of PMSMs. The transformation converts balanced three-phase quantities into balanced two-phase quadrature quantities and then into a rotating rotor reference frame. Field-oriented control (FOC) is implemented to achieve high-performance and efficient control. The model is developed in the *dq*-axis reference frame and includes second-order polynomial functions to account for magnetic saturation effects on the inductances. The chapter also presents a decoupled scheme for parameter estimation that reduces cross-coupling effects and computational burden.

Chapter 3 explores deterministic and stochastic optimization algorithms, presenting their advantages and limitations. It investigates Particle Swarm

Optimization and its variants, as well as Genetic Algorithm. The Constriction Coefficient-Based PSO (CCPSO) is developed using three main objective functions, which decouple multiparameter estimation. The validity of the proposed method is then experimentally verified using a three-phase laboratory IPMSM. The results demonstrate the accuracy and efficiency of the proposed method in estimating the winding resistance, PM flux linkage, and *dq*-axis inductances under various operating conditions. The proposed method is compared with LS estimation and is found to have higher accuracy.

Chapter 4 presents a parameter-independent model for the MTPA control of PMSMs that aims to maximize torque output for a specific current level while minimizing the magnitude of the stator current. This model utilizes the gradient descent algorithm for an optimal current angle search and considers nonlinearities to eliminate the requirement for online parameter estimation. The model uses the *dq*-axis voltage and current values to calculate the electromagnetic torque equation, and VSI nonlinearity effects are incorporated into the voltage equations.

Chapter 5 discusses techniques for designing experiments and implementing the Taguchi method to carry out experiments that utilize orthogonal arrays to enhance the quality and reliability of the testing process while minimizing inconsistencies. The experimental design considered three primary factors affecting the parameters, including temperature, load torque, and speed, each with varying levels. The acquired data are used to analyze the impact of these factors on the parameters and their sensitivities.

Chapter 6 is the conclusion chapter, summarizing all the research work and contributions made toward achieving the research objectives. Future work to continue this research is also presented.

1.8. References

[1] J.A. Sanguesa, V. Torres-Sanz, P. Garrido, F.J. Martinez, and J.M. Marquez-Barja, "A Review on Electric Vehicles: Technologies and Challenges," Smart Cities, vol. 4, pp. 372-404, 2021. [Online]. Available: https://doi.org/10.3390/smartcities4010022

[2] X. Sun, Z. Li, X. Wang, and C. Li, "Technology Development of Electric Vehicles: A Review," Energies, vol. 13, p. 90, 2020. https://doi.org/10.3390/en13010090

[3] Global EV Sales for 2022, [online], Available: https://www.ev-volumes.com/

[4] Hu, Xiaosong, *et al*. "Powertrain Design and Control in Electrified Vehicles: A Critical Review." *IEEE Transactions on Transportation Electrification*, vol. 7, no. 3, Sept. 2021, pp. 1990–2009, https://doi.org/10.1109/tte.2021.3056432.

[5] "Car Drivetrain Diagram | My Wiring Diagram." Detoxicrecenze.com, 23 July 2018, detoxicrecenze.com/car-drivetrain-diagram/.

[6] A. Emmanuel, et al. "An Overview of Electric Machine Trends in Modern Electric Vehicles." *Machines*, vol. 8, no. 2, 17 Apr. 2020, p. 20, https://doi.org/10.3390/machines8020020

[7] Yang, Zhi, et al. "Comparative Study of Interior Permanent Magnet, Induction, and Switched Reluctance Motor Drives for EV and HEV Applications." *IEEE Transactions on Transportation Electrification*, vol. 1, no. 3, 1 Oct. 2015, pp. 245–254, ieeexplore.ieee.org/document/7210190.

[8] M. S. Rafaq and J. -W. Jung, "A comprehensive review of state-of-the-art parameter estimation techniques for permanent magnet synchronous motors in wide speed range, "*IEEE Trans. Industr. Inform.*, vol. 16, no. 7, pp. 4747-4758, July 2020.

[9] Z. Q. Zhu, D. Liang, and K. Liu, "Online parameter estimation for permanent magnet synchronous machines: An overview," IEEE Access, vol. 9, pp. 59059-59084, 2021.

[10] K. Liu, Z. Q. Zhu, Q. Zhang, and J. Zhang, "Influence of nonideal voltage measurement on parameter estimation in permanent-magnet synchronous machines," *IEEE Trans. Ind. Electron.*, vol. 59, no. 6, pp. 2438-2447, June 2012.

[11] Kim, Hag-Wone, et al. "Nonlinearity Estimation and Compensation of PWM VSI for PMSM under Resistance and Flux Linkage Uncertainty." Nonlinearity Estimation and Compensation of PWM VSI for PMSM under Resistance and Flux Linkage Uncertainty, vol. 14, no. 4, 26 June 2006, pp. 589–601.

[12] B. Stumberger, G. Stumberger, D. Dolinar, A. Hamler, and M. Trlep, "Evaluation of saturation and cross-magnetization effects in interior permanent-magnet synchronous motor," *IEEE Trans. Industr. Appl.*, vol. 39, no. 5, pp. 1264-1271, Sept.-Oct. 2003.

[13] A. Dietz, M. Caruso, A. O. Di Tommaso, R. Miceli and C. Nevoloso, "Enhanced Mathematical Modelling of Interior Permanent Magnet Synchronous Machine Considering Saturation, Cross-Coupling and Spatial Harmonics effects," *2020 Fifteenth International Conference on Ecological Vehicles and Renewable Energies (EVER)*, Monte-Carlo, Monaco, 2020, pp. 1-9, doi: 10.1109/EVER48776.2020.9243003.

[14] Sun, Xin, and Xi Xiao. "Precise Non-Linear Flux Linkage Model for Permanent Magnet Synchronous Motors Based on Current Injection and Bivariate Function Approximation." *Precise Non-Linear Flux Linkage Model for Permanent Magnet Synchronous Motors Based on Current Injection and Bivariate Function Approximation*, vol. 14, no. 11, 10 Aug. 2020, pp.2044–2050.

[15] Feng, Guodong, Chunyan Lai, and Narayan C. Kar. "A novel current injection-based online parameter estimation method for PMSMs considering magnetic saturation." *IEEE Transactions on Magnetics* 52.7 (2016): 1-4.

[16] Feng, Guodong, et al. "Current injection-based online parameter and VSI nonlinearity estimation for PMSM drives using current and voltage DC components." *IEEE Transactions on Transportation Electrification* 2.2 (2016): 119-128.

[17] Li, Ze, et al. "Current injection-based multi-parameter estimation for dual three-phase IPMSM considering VSI nonlinearity." *IEEE Transactions on Transportation Electrification* 5.2 (2019): 405-415.

[18] Li, Ze, et al. "Current Injection-based Simultaneous Stator Winding and PM Temperature Estimation for Dual Three-phase PMSMs." *IEEE Transactions on Industry Applications* (2021).

[19] Li, Ze, et al. "Investigation of on-Line Parameter Estimation for Interior PMSMs Considering Current Injection and Machine Operating Conditions." *2018 21st International Conference on Electrical Machines and Systems (ICEMS)*. IEEE, 2018.

[20] Liu, Kan, et al. "Online multiparameter estimation of nonsalient-pole PM synchronous machines with temperature variation tracking." *IEEE Transactions on Industrial Electronics* 58.5 (2010): 1776-1788.

[21] Liu, Kan, Zi-Qiang Zhu, and David A. Stone. "Parameter estimation for condition monitoring of PMSM stator winding and rotor permanent magnets." *IEEE Transactions on Industrial Electronics* 60.12 (2013): 5902-5913.

[22] Liu, Zhao-Hua, et al. "Parameter estimation for VSI-fed PMSM based on a dynamic PSO with learning strategies." *IEEE Transactions on Power Electronics* 32.4 (2016): 3154-3165.

[23] Liu, Kan, and Zi-Qiang Zhu. "Position offset-based parameter estimation for permanent magnet synchronous machines under variable speed control." *IEEE Transactions on Power Electronics* 30.6 (2014): 3438-3446.

[24] Liu, Kan, and Zi-Qiang Zhu. "Position-offset-based parameter estimation using the Adaline NN for condition monitoring of permanent-magnet synchronous machines." *IEEE Transactions on Industrial Electronics* 62.4 (2014): 2372-2383.

[25] Liu, Kan, and Zi-Qiang Zhu. "Mechanical parameter estimation of permanent-magnet synchronous machines with aiding from estimation of rotor PM flux linkage." *IEEE Transactions on Industry Applications* 51.4 (2015): 3115-3125.

CHAPTER 2

Enhanced Mathematical Model of PMSM Accounting for Nonlinearities

2.1. Introduction

Accurate PMSM parameter estimation is essential for designing high-quality and reliable controllers and enhancing motor performance. The electrical parameters, including the stator winding resistance, PM flux linkage, and d- and q-axis inductances, are sensitive to mechanical vibrations and variations in operating conditions, such as load, speed, and temperature. Due to magnetic saturation, the dq-axis inductances exhibit significant variations in response to changes in load torque or current. Temperature has a considerable influence on stator resistance and PM flux linkage. Moreover, there is a nonlinear voltage gain between the reference voltages from the output of the PI controllers and the actual motor terminal voltages due to the nonideal characteristics of the PWM-fed VSI. Ignoring this VSI nonlinearity causes significant error in the estimated parameters. Therefore, in this chapter, VSI nonlinearity is modeled for a three-phase IPMSM and included in the dq-axis reference frame voltage equations. In addition, the inductances are modeled using second-order polynomial functions accounting for self- and cross-saturation effects, and a mathematical model for the multiparameter estimation of IPMSMs considering nonlinearities is presented. Since cross-coupling effects exist between parameters that may cause estimation errors, a decoupled scheme is proposed to reduce both the cross-coupling effects and computational burden of the estimation process.

2.2. Clarke-Park Transformation

Voltage and current equations are commonly used to describe the PMSM dynamic behavior. Except for the case of a stationary rotor, the coefficients in the differential equations regulate their behavior changes over time. Given the continuous variation in flux linkages, induced voltages, and currents during relative motion within an electric circuit, the mathematical modeling of such systems tends to be complex. Mathematical transformations are commonly used in electrical-machine analysis to address this complexity. By aligning all variables to a single frame of reference, these transformations help decouple the variables and solve equations involving time-varying quantities. For

PMSMs, the process involves initiating a Clarke transformation to convert balanced three-phase quantities into balanced two-phase quadrature quantities. Following this, Park transformation is employed to convert these orthogonal two-phase vectors from a stationary stator frame to a rotating rotor reference frame. The Clarke-Park transformation simplifies the control and analysis of PMSMs and is essential for most common control techniques, such as FOC, direct torque control (DTC), and model predictive control (MPC) [1]. The Clarke-Park transformation can be formulated as:

$$
\begin{bmatrix} f_\alpha \\ f_\beta \end{bmatrix} = \frac{2}{3} \begin{bmatrix} 1 & -\frac{1}{2} & -\frac{1}{2} \\ 0 & \frac{\sqrt{3}}{2} & -\frac{\sqrt{3}}{2} \end{bmatrix} \begin{bmatrix} f_a \\ f_b \\ f_c \end{bmatrix}
\tag{2.1}
$$

$$
\begin{bmatrix} f_d \\ f_q \end{bmatrix} = \begin{bmatrix} \cos\theta & \sin\theta \\ -\sin\theta & \cos\theta \end{bmatrix} \begin{bmatrix} f_\alpha \\ f_\beta \end{bmatrix}
\tag{2.2}
$$

$$
\begin{aligned}
\begin{bmatrix} f_d \\ f_q \end{bmatrix} &= \begin{bmatrix} \cos\theta & \sin\theta \\ -\sin\theta & \cos\theta \end{bmatrix} \times \frac{2}{3} \begin{bmatrix} 1 & -\frac{1}{2} & -\frac{1}{2} \\ 0 & \frac{\sqrt{3}}{2} & -\frac{\sqrt{3}}{2} \end{bmatrix} \begin{bmatrix} f_a \\ f_b \\ f_c \end{bmatrix} \\
&= \frac{2}{3} \begin{bmatrix} \cos(\theta) & \cos(\theta - \frac{2\pi}{3}) & \cos(\theta + \frac{2\pi}{3}) \\ -\sin\theta & -\sin(\theta - \frac{2\pi}{3}) & -\sin(\theta + \frac{2\pi}{3}) \end{bmatrix} \begin{bmatrix} f_a \\ f_b \\ f_c \end{bmatrix}
\end{aligned}
\tag{2.3}
$$

In the above equations, f represents the voltage, current, or flux linkage, and θ is the rotor angular position. (2.1) demonstrates the Clarke transformation, which transitions from an *abc* three-phase stator reference frame to an orthogonal two-phase αβ frame. The Park transformation, denoted by (2.2), converts the αβ coordinates to the *dq* rotating rotor reference frame. Finally, (2.3) denotes the Clarke-Park transformation, enabling the conversion of *abc* coordinates to the *dq* reference frame. The vector representations of all aforementioned reference frames are illustrated in Fig. 2.1.
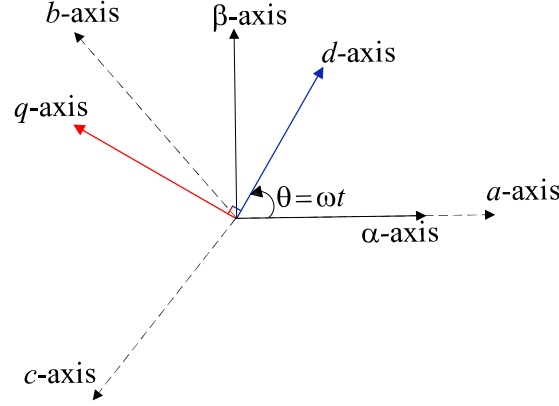
Fig. 2.1. Combined vector representation of all reference frames.

2.3. Field-Oriented Control for PMSM Drives

FOC, or Vector Control (VC), is the most common control strategy for PMSM and other synchronous machines to achieve high-performance and efficient control. Its main goal is to decouple the motor control into two independent orthogonal components: magnetic torque and magnetic flux as much as possible [2], [3]. The voltage and flux linkage equations for a conventional three-phase PMSM in an *abc* frame can be described as follows:

$$\left. \begin{aligned} v_{abc} &= R_s i_{abc} + \dot{\lambda}_{abc} \\ \lambda_{abc} &= L i_{abc} + \lambda_{PM,abc} \end{aligned} \right\} \tag{2.4}$$

Transforming the machine model into a rotating *dq* reference frame simplifies the control by projecting AC quantities into DC quantities. By performing the Clarke-Park transformation, the voltage equations can be represented as:

$$\left. \begin{aligned} v_d &= R_s i_d + L_d \frac{di_d}{dt} - \omega_e L_q i_q \\ v_q &= R_s i_q + L_q \frac{di_q}{dt} + \omega_e \left(L_d i_d + \lambda_{PM} \right) \end{aligned} \right\} \tag{2.5}$$

The torque of the PMSM is generated by the interaction between the magnetic fields of the stator and the rotor. The magnetic field of the rotor is defined by the magnetic flux of the PMs and remains relatively constant, except for the field-weakening operation. The stator magnetic field is represented by stator current. To achieve maximum torque output,

21

the stator current vector should be controlled such that it is perpendicular to the rotor magnetic field. Furthermore, in IPMSMs, an additional torque, known as reluctance torque, is generated due to the variation in reluctance between the stator and rotor poles during rotor rotation. The cumulative torque generated in the IPMSM is expressed as:

$$\tau_e = 1.5P[\lambda_{PM}i_q + (L_d - L_q)i_d i_q] \tag{2.6}$$

Figure 2.2 depicts the FOC block diagram for the PMSM, including both the speed and current control loops. The reference currents are compared with the actual feedback signals obtained by the current sensors to measure the current error and feed them as inputs to two PI controllers to provide *dq*-axis voltages. Current controllers are typically of the PI type because of their fast dynamic response; however, alternative types of complex controllers can also be employed to achieve optimal, robust, and adaptive control. The *dq*-axis voltages are subsequently converted to *abc*-axis voltages and fed into a PWM system to generate gating signals for the inverter. The VSI inverts the DC input power to a three-phase AC output that supplies PMSM. The machine develops an accurate torque based on the applied voltages and currents and rotates at a speed corresponding to its own inertia and load. The rotor position signal is used to calculate the actual speed. Through the speed controller within the FOC, the motor speed is adjusted to the speed command by comparing it with the feedback, which calculates the error to update the speed PI controller and generates a *q*-axis current command.
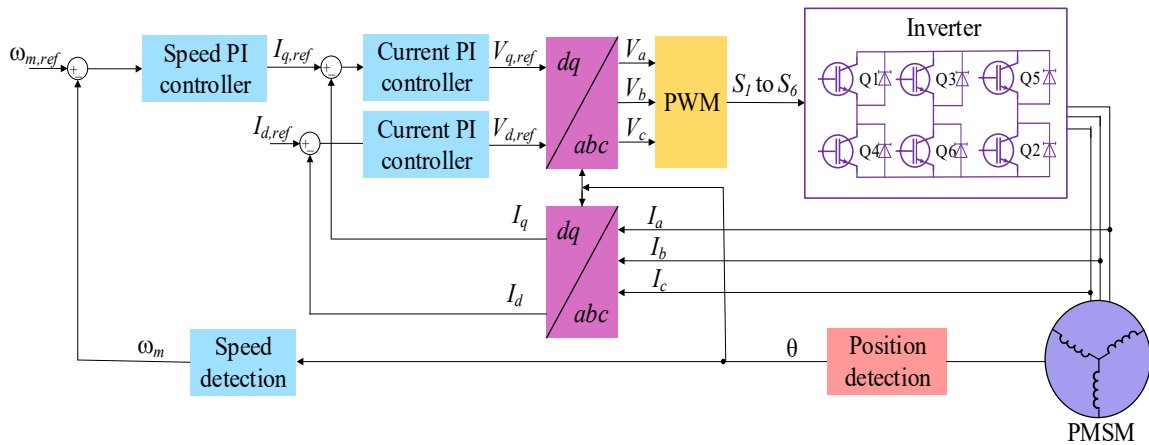
Fig. 2.2. Overview block diagram of field-oriented control for PMSM.

22

2.4. PWM VSI Nonlinearity Modeling for Three-Phase PMSM

In PMSM drives, inverter control significantly affects both the performance and the overall state of health (SoH). In VSIs, the pulse-width modulation (PWM) technique is widely used for motor control to achieve variable frequencies and voltages from a fixed DC voltage obtained using switching devices. Figure 2.3 illustrates a three-phase two-level PWM VSI, which is constructed with six switches and connected to the PMSM load.
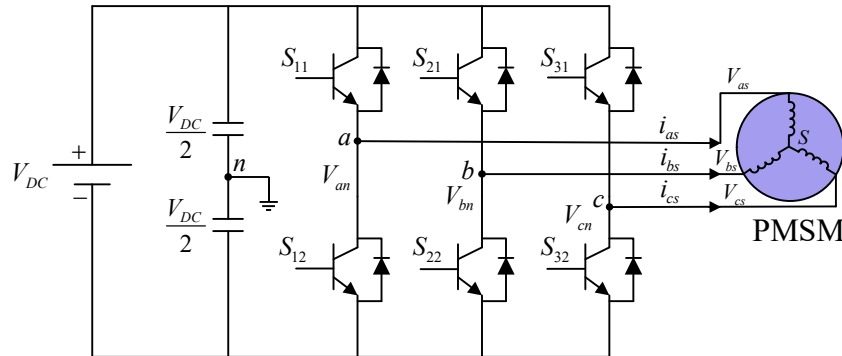
Fig. 2.3. Schematic of a three-phase two-level VSI.

Table 2.1 represents the switching states of the VSI consisting of eight switching states, ensuring that two switches on the same leg operate complementarily and are not simultaneously turned ON.

TABLE 2.1
SWITCHING STATES IN A THREE-PHASE TWO-LEVEL INVERTER

State #	S_{11}	S_{12}	S_{31}	V_{ab}	V_{bc}	V_{ca}
1	0	0	0	0	0	0
2	0	0	1	0	$-V_{DC}$	V_{DC}
3	0	1	0	$-V_{DC}$	V_{DC}	0
4	0	1	1	$-V_{DC}$	0	$-V_{DC}$
5	1	0	0	V_{DC}	0	$-V_{DC}$
6	1	0	1	V_{DC}	$-V_{DC}$	0
7	1	1	0	0	V_{DC}	$-V_{DC}$
8	1	1	1	0	0	0

2.4.1. Sinusoidal PWM in Three-Phase VSI

Sinusoidal PWM (SPWM) generates inverter gating signals by comparing the very-high-frequency carrier wave with three-phase sine waves shifted by 120° with the frequency of the desired output voltage. The main disadvantage of SPWM is that it contains high harmonic content, resulting in an increase in the total harmonic distortion (THD) in

the output sine waveform [4]–[7]. Figure 2.4 illustrates the switching pulses generated by SPWM and its performance by comparing the sine waveform and carrier signal, which may be in the form of a sawtooth or triangle wave. Figure 2.5 exhibits the generated output line-to-line voltage of the VSI.
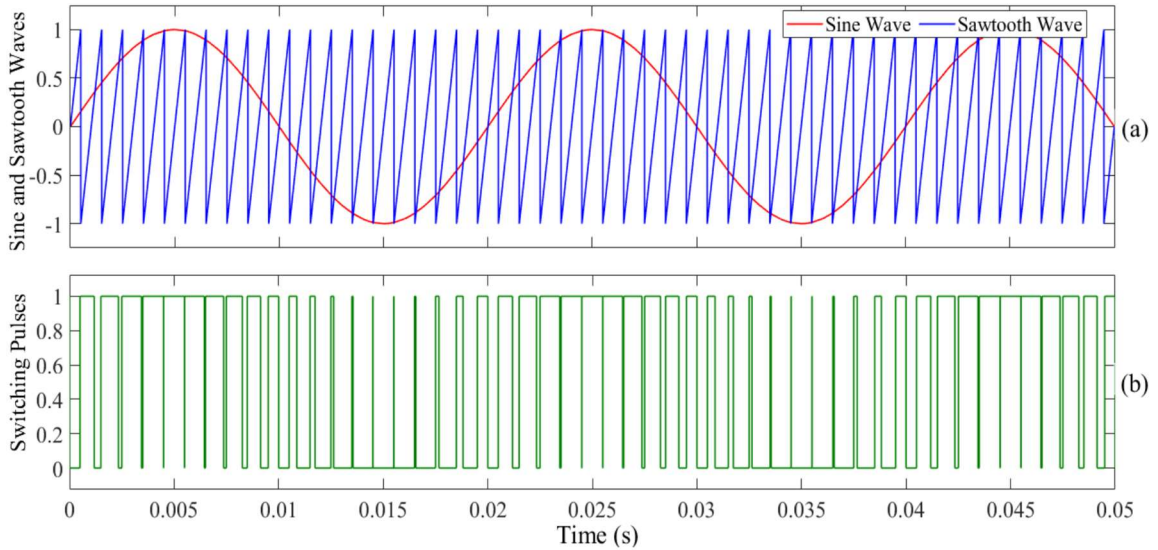
Fig. 2.4. SPWM performance illustration. (a) Comparing sine wave and carrier sawtooth wave. (b) Switching pulses of one switch.
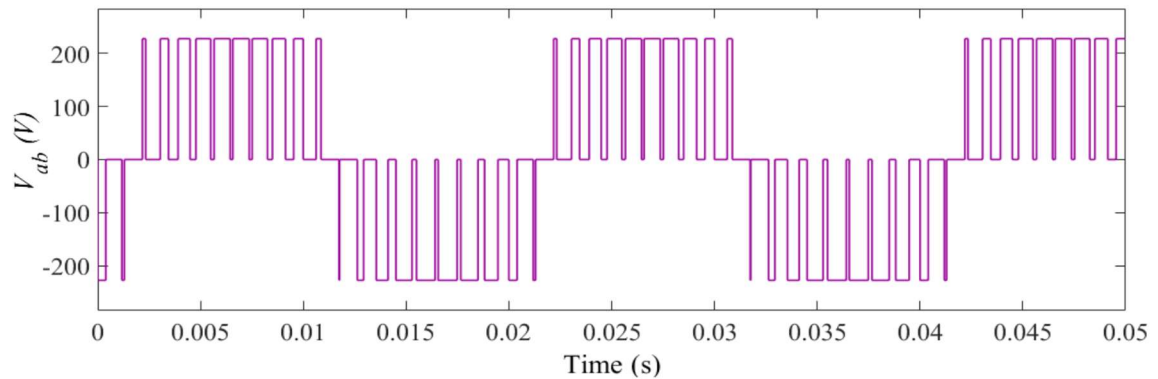
Fig. 2.5. Line-to-line output voltage waveform of SPWM VSI.

2.4.2. VSI Nonlinearity Modeling and Compensation

In the control of PMSMs within the FOC system, direct measurement of terminal voltages from the stator winding terminals is usually unfeasible due to the absence of voltage sensors. Therefore, reference voltages, which are the output voltages from PI controllers, are often utilized for parameter estimation. However, the reference voltages

are not equal to the actual voltages due to nonideal voltage measurements or nonlinear voltage gains between the reference and output voltages caused by the DC bus voltage drop, zero shift in the amplifier, and VSI nonlinearities such as dead time and nonideal inherent characteristics of the power switches. These nonideal characteristics may vary under various operating conditions, such as current, temperature, and DC bus voltage and introduce current distortions, torque ripple, and instability of the control system [8], [9]. Neglecting VSI nonlinearity hugely affects the accuracy of estimated parameters and potentially leads to a significant error.
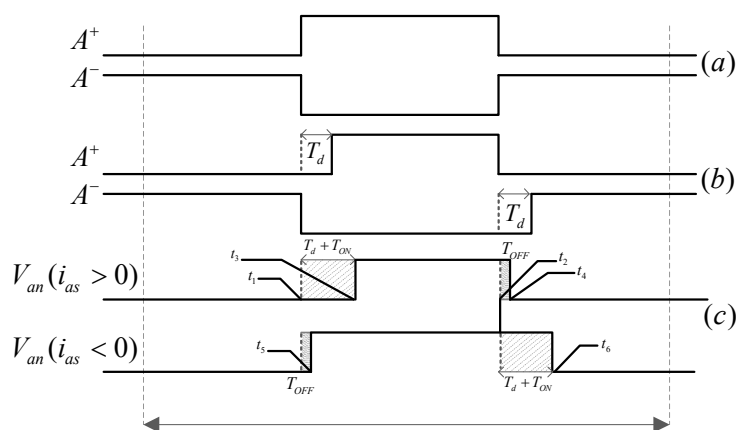
Fig. 2.6. IGBT drive signal for inverter output voltage. (a) Ideal IGBT drive signal. (b) Actual IGBT drive signal including dead time. (c) Actual IGBT drive signal including dead time and switch on/off times.

Figure 2.6 shows the ideal and actual IGBT drive signals for phase A of a three-phase PWM inverter. The reference voltage is the area between t_1 and t_2, whereas the actual voltage is the area between t_3 and t_4 ($i_{as} > 0$) or t_5 and t_6 ($i_{as} < 0$), considering the dead time and conducting time delay of the switch. The voltage error depends on the phase current and the lengths of T_{ON}, T_d, and T_{OFF}. In [10], it states that the output actual voltage of phase A can be derived using (2.7), where E is the error due to nonideal switching. The equations are as follows:

$$V_{an} = V_{an}^* + \text{sign}(i_{as})E \tag{2.7}$$

where,
$$\text{sign}(i_{as}) = \begin{cases} 1, & i_{as} \geq 0 \\ -1, & i_{as} < 0 \end{cases} \tag{2.8}$$

25

The relationship between the commanded time ($T_a{}^*$) and actual time (T_a) durations of PWM is as follows. M is the total time error calculated by (2.10):

$$T_a = T_a^* + \text{sign}(i_{as})M \tag{2.9}$$

$$M = T_{com} + T_{OFF} - T_{ON} - T_d \tag{2.10}$$

As suggested in [10], T_{com} can be adjusted to eliminate the distorted voltage, and the actual phase voltage can be obtained using (2.11), where r_{ce} and r_d are the ON-state resistances of the active switch and freewheeling diode, respectively.

$$V_{as} = V_{as}^* + V_{as}' - \frac{1}{2}(r_{ce} + r_d)i_{as} \tag{2.11}$$

$$V_{as}' = \frac{1}{6}\left(V_{DC}\frac{M}{T_s} - V_{ce0} - V_{d0}\right) \times (2\text{sign}(i_{as}) - \text{sign}(i_{bs}) - \text{sign}(i_{cs})) \tag{2.12}$$

V_{as}' is the distorted voltage and can be derived from (2.12). V_{ce0} and V_{d0} are the threshold voltages of the active switch and freewheeling diode, respectively. When V_{as}' equals zero, T_{com}, as well as E, can be derived from (2.13) and (2.14), respectively [8]. The voltages for the other two phases can be similarly achieved.

$$T_{com} = T_d - T_{OFF} + T_{ON} + T_s\frac{V_{ce0} + V_{d0}}{V_{DC}} \tag{2.13}$$

$$E = \frac{-T_{com}}{2T_s}V_{DC} \tag{2.14}$$

As detailed in [13], the steady-state dq-axis equations can be written as in (2.15), where v_d^{err} and u_q^{err} are the distorted voltages due to VSI nonlinearity, v_d and v_q are the reference voltages, and u_d and u_q are the actual voltages.

$$\left.\begin{array}{l} v_d = u_d + v_d^{err} \\ v_q = u_q + v_q^{err} \end{array}\right\} \tag{2.15}$$

$$\left.\begin{array}{l} v_d^{err} = D_d V_{dead} + r_{cd}i_d - U\sin\varphi \\ v_q^{err} = D_q V_{dead} + r_{cd}i_q + U\cos\varphi \end{array}\right\} \tag{2.16}$$

26

The distorted voltage consists of three parts, as modeled in (2.16). r_{cd} is the equivalent ON-state resistance of the active switch and the freewheeling diode. φ represents the angle between the voltage vector and q-axis. V_{dead} and U denote the distorted voltage terms, and D_d and D_q are the periodic functions of the rotor position (θ) and the current angle (γ), which is the angle between the current vector and q-axis, expressed as follows:

$$D_d = 2\sin\left[\theta - \mathrm{int}\left\{3\left(\theta + \gamma + \frac{\pi}{6}\right)\Big/\pi\right\} \times \frac{\pi}{3}\right]$$
$$D_q = 2\cos\left[\theta - \mathrm{int}\left\{3\left(\theta + \gamma + \frac{\pi}{6}\right)\Big/\pi\right\} \times \frac{\pi}{3}\right]$$

(2.17)

In $\{x\}$, function takes the nearest integer x. Upon incorporating the distorted voltage terms into the steady-state PMSM equations, (2.18) yields.

$$\left.\begin{aligned} v_d &= (R_s + r_{cd})i_d - \omega_e L_q i_q + D_d V_{dead} - U\sin\varphi \\ v_q &= (R_s + r_{cd})i_q + \omega_e L_d i_d + \omega_e \lambda_{PM} + D_q V_{dead} + U\cos\varphi \end{aligned}\right\}$$

(2.18)

In real applications, $(r_{ce}+r_d)$ or r_{cd} is considered part of the stator winding resistance, which is why the estimated resistance is usually greater than the actual resistance. Moreover, the distorted voltage term V_{dead} is much greater than U; thus, U can be neglected, and the equations can be simplified as follows:

$$\left.\begin{aligned} v_d &= R_s i_d - \omega_e L_q i_q + D_d V_{dead} \\ v_q &= R_s i_q + \omega_e L_d i_d + \omega_e \lambda_{PM} + D_q V_{dead} \end{aligned}\right\}$$

(2.19)

As can be seen from (2.17), D_d and D_q are functions of both the rotor position (θ) and the current angle (γ). The rotor position changes from 0° to 360°. Figure 2.7 depicts the distorted coefficients under two different current angles 0° and 20° with respect to the rotor position.

To prevent any potential position signal error and simplicity, [12] suggested using the average values of D_d and D_q and saving it as a lookup table for parameter estimation. The mean values which are independent of rotor position can be obtained using (2.20). Figure

2.8 represents the mean values of the distorted coefficients, denoted as D_D and D_Q, under various current angles from 0° to 90°.

$$
\left.\begin{aligned}
D_D &= \frac{1}{N}\sum_{k=1}^{N}2\sin\left[\theta - \mathrm{int}\left\{3\left(\theta+\gamma+\frac{\pi}{6}\right)\Big/\pi\right\}\times\frac{\pi}{3}\right] \\
D_Q &= \frac{1}{N}\sum_{k=1}^{N}2\cos\left[\theta - \mathrm{int}\left\{3\left(\theta+\gamma+\frac{\pi}{6}\right)\Big/\pi\right\}\times\frac{\pi}{3}\right]
\end{aligned}\right\}
\tag{2.20}
$$
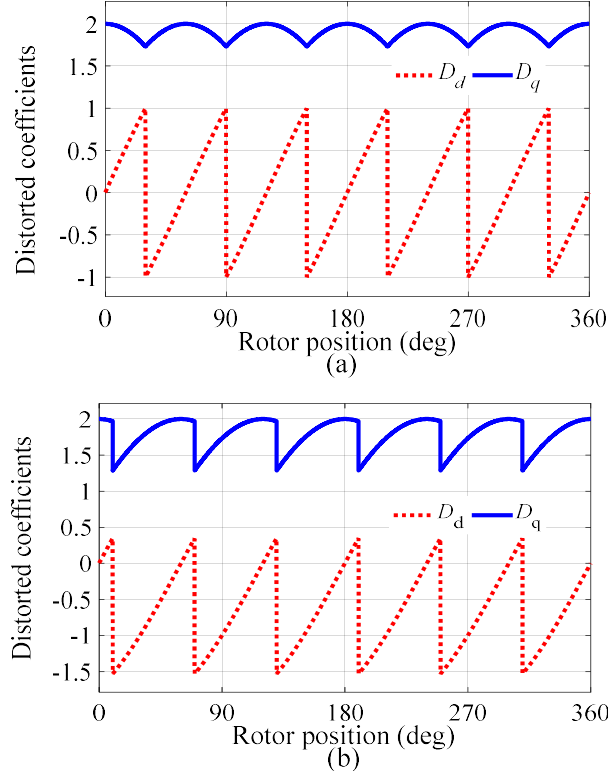
Fig. 2.7. Waveforms of distorted coefficients D_d and D_q with respect to rotor position at two different current angles. (a) γ=0°. (b) γ=20°.

In [8], it is revealed that both the PM flux linkage and stator winding resistance estimations are greatly influenced by VSI nonlinearity compensation at low speeds; however, at high speeds, only the winding resistance estimation is significantly influenced, and the PM flux linkage estimation is barely affected.
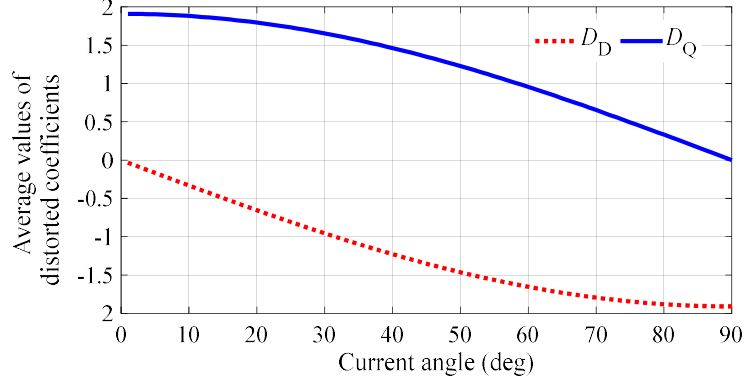
Fig. 2.8. Average values of distorted coefficients, denoted as D_D and D_Q at various current angles.

2.5. PMSM Modeling Considering Magnetic Saturation and VSI Nonlinearity

In an actual PMSM, inductances vary nonlinearly with variations in loads or currents due to magnetic saturation. In a three-phase PMSM, the *dq*-axis inductances can be modeled as functions of the *dq*-axis currents, as expressed in (2.21). Neglecting magnetic saturation can deteriorate the parameter estimation and result in inaccurate parameters. Second-order polynomial functions, as denoted by (2.22), represent the nonlinear relationships between inductances and currents, which can be used to model this nonlinearity over a wide range of operating conditions.

$$\left.\begin{array}{l} L_d = f_d(i_d, i_q) \\ L_q = f_q(i_d, i_q) \end{array}\right\} \tag{2.21}$$

$$\left.\begin{array}{l} L_d\left(i_d, i_q\right) = L_{d0} + \alpha_1 i_d + \alpha_2 i_q + \alpha_3 i_d^2 + \alpha_4 i_q^2 + \alpha_5 i_d i_q \\ L_q\left(i_d, i_q\right) = L_{q0} + \beta_1 i_d + \beta_2 i_q + \beta_3 i_d^2 + \beta_4 i_q^2 + \beta_5 i_d i_q \end{array}\right\} \tag{2.22}$$

where L_{d0} and L_{q0} are unsaturated *dq*-axis inductances, and α_1 to α_5 and β_1 to β_5 are the saturation coefficients of the *d*- and *q*-axis inductances in the polynomial model, respectively. When the coefficients are equal to zero, the model is a linear equation without considering magnetic saturation. By inserting (2.22) into (2.19) and integrating magnetic saturation as well as VSI nonlinearity withing the mathematical model of PMSM, the subsequent equations are obtained:

29

$$v_d = R_s i_d - \omega_e L_q \left(i_d, i_q \right) i_q + D_d V_{dead}$$
$$v_q = R_s i_q + \omega_e L_d \left(i_d, i_q \right) i_d + \omega_e \lambda_{PM} + D_q V_{dead} \qquad (2.23)$$

$$v_d = R_s i_d - \omega_e (L_{q0} + \beta_1 i_d + \beta_2 i_q + \beta_3 i_d^2 + \beta_4 i_q^2 + \beta_5 i_d i_q) i_q + D_d V_{dead}$$
$$v_q = R_s i_q + \omega_e (L_{d0} + \alpha_1 i_d + \alpha_2 i_q + \alpha_3 i_d^2 + \alpha_4 i_q^2 + \alpha_5 i_d i_q) i_d + \omega_e \lambda_{PM} + D_q V_{dead} \qquad (2.24)$$

Given the inevitable rotor position error, the averaging of D_d and D_q in each electrical cycle, represented as D_D and D_Q, computed from (2.20), as exemplified in Fig. 2.8 is employed for parameter estimation. Additionally, in this study, the DC components of the *dq*-axis voltage and current measurements are used, which function as a filter to reduce measurement noise and enhance parameter estimation. These average measurements can be calculated using (2.25) and (2.26).

$$V_d = \frac{1}{N} \sum_{k=1}^{N} v_d(k)$$
$$V_q = \frac{1}{N} \sum_{k=1}^{N} v_q(k) \qquad (2.25)$$

$$I_d = \frac{1}{N} \sum_{k=1}^{N} i_d(k)$$
$$I_q = \frac{1}{N} \sum_{k=1}^{N} i_q(k) \qquad (2.26)$$

Substituting (2.25), (2.26) and (2.20) into (2.24) yields the full DC-component-based PMSM model for parameter estimation expressed as follows:

$$V_d = R_s I_d - \omega_e (L_{q0} + \beta_1 I_d + \beta_2 I_q + \beta_3 I_d^2 + \beta_4 I_q^2 + \beta_5 I_d I_q) I_q + D_D V_{dead}$$
$$V_q = R_s I_q + \omega_e (L_{d0} + \alpha_1 I_d + \alpha_2 I_q + \alpha_3 I_d^2 + \alpha_4 I_q^2 + \alpha_5 I_d I_q) I_d + \omega_e \lambda_{PM} + D_Q V_{dead} \qquad (2.27)$$

Figure 2.9 illustrates the PMSM vector diagram in the *dq*-axis reference frame, incorporating the magnetic saturation and VSI nonlinearity models.
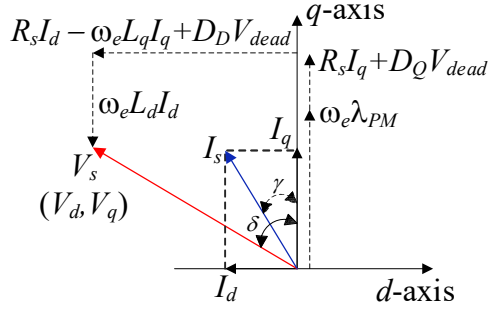
Fig. 2.9. PMSM vector diagram in *dq*-axis reference frame.

2.6. Cross-Coupling Mitigation and Computational Efficiency Through Decoupling

By integrating the magnetic saturation and VSI nonlinearity caused by dead time into the PMSM model, (2.27) is deduced. As observed in (2.27), the model consists of 15 unknown parameters, including R_s, λ_{PM}, V_{dead}, L_{d0}, L_{q0}, α_1 to α_5, and β_1 to β_5, which cannot be estimated from a single operating point due to the rank deficiency of the equations and leads to an ill-convergence problem and inaccurate estimation. In this study, a large amount of data is collected at various speeds and loads to address this issue and accurately estimate all unknown parameters. In addition, to simplify the estimation process, minimize the computational complexity and cross-coupling effects between electrical parameters, and increase the estimation accuracy, a decoupled scheme is proposed [14], [15], which decouples the PMSM steady-state equations into four speed independent variables denoted as X_1, X_2, Y_1, and Y_2, as expressed in (2.28), and decouples the estimation of the parameters from each other. For example, the stator winding resistance is estimated separately from the *d*- and *q*-axis inductances using the decoupled scheme. Hence, any potential error in the resistance estimation does not influence the inductance estimation and vice versa. The defined variables can be included in the PMSM equations, as stated in (2.29).

$$\left.\begin{aligned}
X_1 &= R_s I_d + D_D V_{dead} \\
X_2 &= R_s I_q + D_Q V_{dead} \\
Y_1 &= L_{q0} I_q + \beta_1 I_d I_q + \beta_2 I_q^2 + \beta_3 I_d^2 I_q + \beta_4 I_q^3 + \beta_5 I_d I_q^2 \\
Y_2 &= L_{d0} I_d + \alpha_1 I_d^2 + \alpha_2 I_q I_d + \alpha_3 I_d^3 + \alpha_4 I_q^2 I_d + \alpha_5 I_d^2 I_q + \lambda_{PM}
\end{aligned}\right\} \quad (2.28)$$

$$\left.\begin{aligned}
V_d &= X_1 - \omega_e Y_1 \\
V_q &= X_2 + \omega_e Y_2
\end{aligned}\right\} \quad (2.29)$$

31

The measurements and average calculations of voltages V_d and V_q are collected for $M \times N$ different sets of currents $(I_{d,m}, I_{q,n})$, $m = 1, 2,..., M$ and $n = 1, 2,..., N$ under various speeds $\omega_{e,k}$, $k = 1, 2, ..., K$ from the experiments, as a part of comprehensive motor parameter testing as explained in the next chapter. The data collected are first utilized to estimate the defined speed-independent variables in (2.28) using the least-squares algorithm with the following equations:

$$X_{LS} = (H^T H)^{-1} H^T Y \tag{2.30}$$

where,

$$X_{LS} = \begin{pmatrix} X_{1,m,n} \\ X_{2,m,n} \\ Y_{1,m,n} \\ Y_{2,m,n} \end{pmatrix}, \ H = \begin{pmatrix} 1 & 0 & -\omega_{e,1} & 0 \\ 0 & 1 & 0 & \omega_{e,1} \\ \vdots & \vdots & \vdots & \vdots \\ 1 & 0 & -\omega_{e,K} & 0 \\ 0 & 1 & 0 & \omega_{e,K} \end{pmatrix}, \ Y = \begin{pmatrix} V_{d,m,n,1} \\ V_{q,m,n,1} \\ \vdots \\ V_{d,M,N,K} \\ V_{q,M,N,K} \end{pmatrix} \tag{2.31}$$

In the following chapter, a computationally efficient estimation scheme that utilizes the CCPSO algorithm is presented. The issue of rank deficiency is addressed by collecting redundant data measurements under various speeds and loads from experiments and accurately estimating the electrical parameters. The nonlinear magnetic saturation model will be employed for inductance estimation, and the effects of VSI nonlinearity caused by dead time will be considered. Furthermore, accuracy and error analyses will be conducted by comparing the estimated and measured parameters.

2.7. Conclusion

In this chapter, the enhanced PMSM mathematical model is derived by incorporating magnetic saturation and VSI nonlinearity. Due to the voltage drops in the power-switching devices, the reference voltages from the output of the PI controllers are not equal to the actual applied voltages on the machine, which deteriorates parameter estimation. Therefore, the distorted voltage caused by the PWM-fed VSI is considered, and a DC-component-based model is proposed to eliminate the rotor position error, improve the accuracy of parameter estimation, and reduce the computational cost. The *dq*-axis inductances are defined by second-order polynomial functions representing their variation

with the stator currents, which can model this nonlinear behavior over a wide range of operating conditions. Finally, a novel decoupled multiparameter scheme is developed that decouples the model into four defined variables that can improve the parameter estimation performance by reducing the cross-coupling effects between the parameters and the computational load.

2.8. References

[1] Krause, Paul C, et al. *Analysis of Electric Machinery and Drive Systems*. Hoboken, New Jersey, Wiley, 2013.

[2] Sadegh Vaez-Zadeh. Control of Permanent Magnet Synchronous Motors. Oxford, Oxford University Press, 2018.

[3] PMSM Control, NXP, https://www.nxp.com/applications/industrial/aerospace-and-mobile-robotics.

[4] Kim, Sang-Hoon. *Electric Motor Control: DC, AC and BLDC Motors*. Cambridge, Massachusetts, Elsevier, 2017.

[5] M. A. Al-Hitmi, S. Moinoddin, A. Iqbal, K. Rahman and M. Meraj, "Space vector vs. sinusoidal carrier-based pulse width modulation for a seven-phase voltage source inverter," in *CPSS Transactions on Power Electronics and Applications*, vol. 4, no. 3, pp. 230-243, Sept. 2019, doi: 10.24295/CPSSTPEA.2019.00022.

[6] X. Zhang, X. Wu, C. Geng, X. Ping, S. Chen and H. Zhang, "An Improved Simplified PWM for Three-Level Neutral Point Clamped Inverter Based on Two-Level Common-Mode Voltage Reduction PWM," in *IEEE Transactions on Power Electronics*, vol. 35, no. 10, pp. 11143-11154, Oct. 2020, doi: 10.1109/TPEL.2020.2978724.

[7] A. M. Hava and E. Ün, "Performance Analysis of Reduced Common-Mode Voltage PWM Methods and Comparison with Standard PWM Methods for Three-Phase Voltage-Source Inverters," in *IEEE Transactions on Power Electronics*, vol. 24, no. 1, pp. 241-252, Jan. 2009, doi: 10.1109/TPEL.2008.2005719.

[8] Kim, Hag-Wone, et al. "Nonlinearity Estimation and Compensation of PWM VSI for PMSM under Resistance and Flux Linkage Uncertainty." Nonlinearity Estimation and

Compensation of PWM VSI for PMSM under Resistance and Flux Linkage Uncertainty, vol. 14, no. 4, 26 June 2006, pp. 589–601.

[9] K. Liu, Z. Q. Zhu, Q. Zhang, and J. Zhang, "Influence of nonideal voltage measurement on parameter estimation in permanent-magnet synchronous machines," IEEE Trans. Ind. Electron., vol. 59, no. 6, pp. 2438-2447, June 2012.

[10] Jong-Woo Choi and S. -K. Sul, "Inverter output voltage synthesis using novel dead time compensation," in *IEEE Transactions on Power Electronics*, vol. 11, no. 2, pp. 221-227, March 1996, doi: 10.1109/63.486169.

[11] A. R. Munoz and T. A. Lipo, "On-line dead-time compensation technique for open-loop PWM-VSI drives," in *IEEE Transactions on Power Electronics*, vol. 14, no. 4, pp. 683-689, July 1999, doi: 10.1109/63.774205.

[12] Feng, Guodong, et al. "Current injection-based online parameter and VSI nonlinearity estimation for PMSM drives using current and voltage DC components." *IEEE Transactions on Transportation Electrification* 2.2 (2016): 119-128.

[13] Li, Ze, et al. "Current injection-based multi-parameter estimation for dual three-phase IPMSM considering VSI nonlinearity." *IEEE Transactions on Transportation Electrification* 5.2 (2019): 405-415.

[14] C. Lai, G. Feng, Z. Li and N. C. Kar, "Computation-Efficient Decoupled Multiparameter Estimation of PMSMs From Massive Redundant Measurements," in *IEEE Transactions on Power Electronics*, vol. 35, no. 10, pp. 10729-10740, Oct. 2020, doi: 10.1109/TPEL.2020.2980315.

[15] S. Etemadi, H. Cheng, M. S. Toulabi, U. Deshpande and N. C. Kar, "Multiparameter Estimation Accuracy Improvement for PMSMs Using a Constriction Coefficient-Based Particle Swarm Optimization," 2023 *IEEE* 32*nd International Symposium on Industrial Electronics (ISIE)*, Helsinki, Finland, 2023, pp. 1-6, doi: 10.1109/ISIE51358.2023.10227963.

CHAPTER 3

Novel Multiparameter Estimation Scheme for PMSMs Using Constriction Coefficient-Based Particle Swarm Optimization

3.1. Introduction

In the last few decades, numerous parameter estimation techniques have been developed for synchronous machines, however, the existence of permanent magnets in rotor and motor nonlinearities requires an effective and robust estimation algorithm that can accurately estimate the parameters. The most common modern estimation algorithms that are extensively implemented for PMSMs include recursive least square (RLS), extended Kalman filter (EKF), model reference adaptive system (MRAS), particle swarm optimization (PSO), genetic algorithms (GA), and neural networks (NN). The choice of efficient and accurate estimation technique and algorithm plays a crucial role in parameter estimation due to inherent nonlinearities and complexities associated with PMSMs. It may depend on different factors, such as the complexity of the motor model, availability of data, computational resources, desired accuracy, and robustness [1].

Due to the linear modeling nature of the RLS algorithm, it is often found unsuitable for nonlinear models such as PMSMs; also, its accuracy can be compromised by noise. Similarly, the EKF algorithm, while employed in studies like [2], for estimating parameters such as the winding resistance and PM flux linkage, is sensitive to noise and instability. MRAS estimator employed in [3], [4] cannot simultaneously estimate all electrical parameters, including stator winding resistance, PM flux linkage, and dq-axis inductances, and requires nominal values of other parameters. NN methods have been widely used recently owing to their high accuracy, however, they usually require a large amount of data for training and additional knowledge for weight adjustment [1], [5].

Metaheuristic optimization algorithms, such as GA and PSO can address the challenges posed by the nonlinearity, complexity, and high dimensionality of PMSM models. In this chapter, a constriction-coefficient-based PSO algorithm is developed using three main objective functions, which decouples the multiparameter estimation. Subsequently, experimental investigations were conducted on a three-phase laboratory IPMSM. The current sweep test was performed at various speeds and currents, and numerous

measurements were collected to solve the rank deficiency and estimate all the electrical parameters, including the winding resistance, PM flux linkage, and *dq*-axis inductances under different operating conditions. Afterward, the results were analyzed to validate the accuracy of the proposed method, the estimated parameters were compared with the measured values, and the error was verified. Finally, comparative analyses were performed to compare the CCPSO-based estimation technique with the LS estimator, in terms of convergence, and accuracy.

3.2. Optimization Algorithms

Parameter identification can be addressed as an optimization problem in which the system response to a known input is used to determine the unknown parameter values of a model. Optimization algorithms can be classified into two main types: deterministic and stochastic algorithms.

Figure 3.1 categorizes the two main types of optimization algorithms and their subsequent classifications [6]. Table 3.1 outlines the strengths and limitations associated with each of these categories [7].
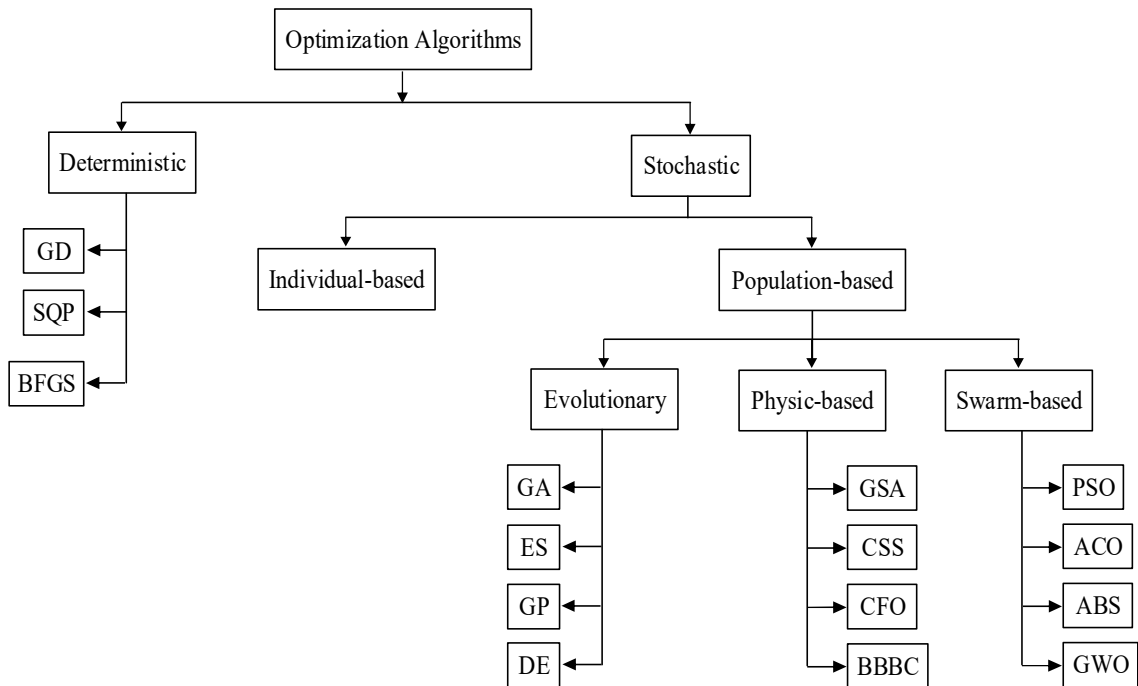
Fig. 3.1. Optimization algorithm classification [6].

Deterministic Algorithms		Stochastic Algorithms	
Advantages	**Drawbacks**	**Advantages**	**Drawbacks**
Reliable in finding the same solution	Local optima stagnation	Avoid local solutions	Slow convergence speed
Require fewer function evaluations	Lower chance of finding the global optimum	Higher chance of finding the global optimum	Finding different answers in each run
Fast convergence	Highly dependent on the initial solution	Less dependent on the initial solution	
	Mostly need a gradient	Mostly do not need a gradient	

3.2.1. Particle Swarm Optimization: Strategy, Flowchart and Variants

PSO is a stochastic iterative population-based optimization algorithm, introduced by Kennedy and Eberhart in 1995 [8]. PSO is a simple, effective, and robust algorithm inspired by the movements of animals, such as flocks of birds and schools of fish that live as swarms. PSO starts with a population of random solutions or so-called particles that modify and improve constantly over the number of iterations. Each particle 'i' is randomly initialized into the search space and can be a potential solution to the optimization problem which has memory and is specified by two vectors of position and velocity. The particle travels in three directions, as illustrated in Fig. 3.2, towards the best outcome discovered by itself so far, known as the personal best, the global best, which is the best experience of the entire swarm and its previous motion or velocity [9]–[11]. The equations for updating the position and velocity can be expressed as:

$$\left.\begin{array}{l} V_{ij}(t+1) = \omega V_{ij}(t) + r_1 c_1 (P_{ij}(t) - X_{ij}(t)) + r_2 c_2 (G_j(t) - X_{ij}(t)) \\ X_{ij}(t+1) = X_{ij}(t) + V_{ij}(t+1) \end{array}\right\} \tag{3.1}$$

The optimization process is propelled by the velocity vector, encompassing both the particle's experience and the information exchanged within its neighborhood. The individual learning of the particle is often termed as the cognitive component, correlating with the distance of the particle from its best-known position (termed as the personal best position or P_{best}) found during the optimization process.
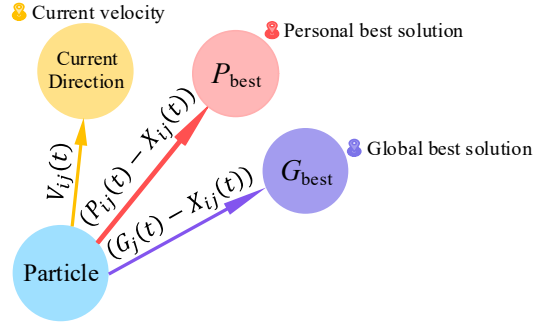
Fig. 3.2. PSO algorithm search strategy.

The socially shared information within the particle's surroundings is denoted as the social component in the velocity equation. In (3.1), $V_{ij}(t)$ represents the velocity of particle i along dimension $j = 1, \ldots, N$ at time step t, and $X_{ij}(t)$ indicates the position of particle i along dimension j at time step t. The positive acceleration constants c_1 and c_2 play a role in scaling the influence of the cognitive and social components, respectively. In addition, the random values r_1 and r_2 are drawn from a uniform distribution $U(0, 1)$. These random values contributed to the stochastic nature of the algorithm [13]. PSO algorithm is controlled by several parameters, including the dimensions of the problem, number of particles, acceleration coefficients (c_1, c_2), inertia weight (ω), population size, number of iterations, and random factors that determine the contribution of cognitive and social components. The inertia weight controls how much the particle remembers its previous velocity. The cognitive component (c_1) controls how much the particle heads toward its personal best position (local search) and the social component (c_2) determines the particles' motion towards the best position found by the entire swarm or the global best position. To smooth the transition and maintain a balance between the exploration (global search) and exploitation (local search) phases of the search mechanism over the course of iterations, these three key parameters; acceleration coefficients, and inertia weight should be adopted appropriately in the velocity update equation. The flowchart of the PSO algorithm is depicted in Fig 3.3, providing an overview of the sequential execution process of PSO.

The standard PSO often fails to converge and entraps in the local optimum. Since the origin of PSO, many studies have focused on improving the performance of PSO by optimizing its parameters, and many variants of PSO have been developed. In one method, linearly decreasing the inertia weight from 0.9 to 0.4, focusing on diversity in the early

iterations and convergence in late iterations [12]. Time-varying PSO (TVPSO) aims to improve global search in the early stages by using a large cognitive parameter and a small social parameter to allow particles to move freely at the beginning. The parameters are being modified during the iterations by reducing the cognitive parameter to a smaller value and increasing the social parameter to a larger value, in order to encourage the particles to converge towards the global optimum in later stages [13].
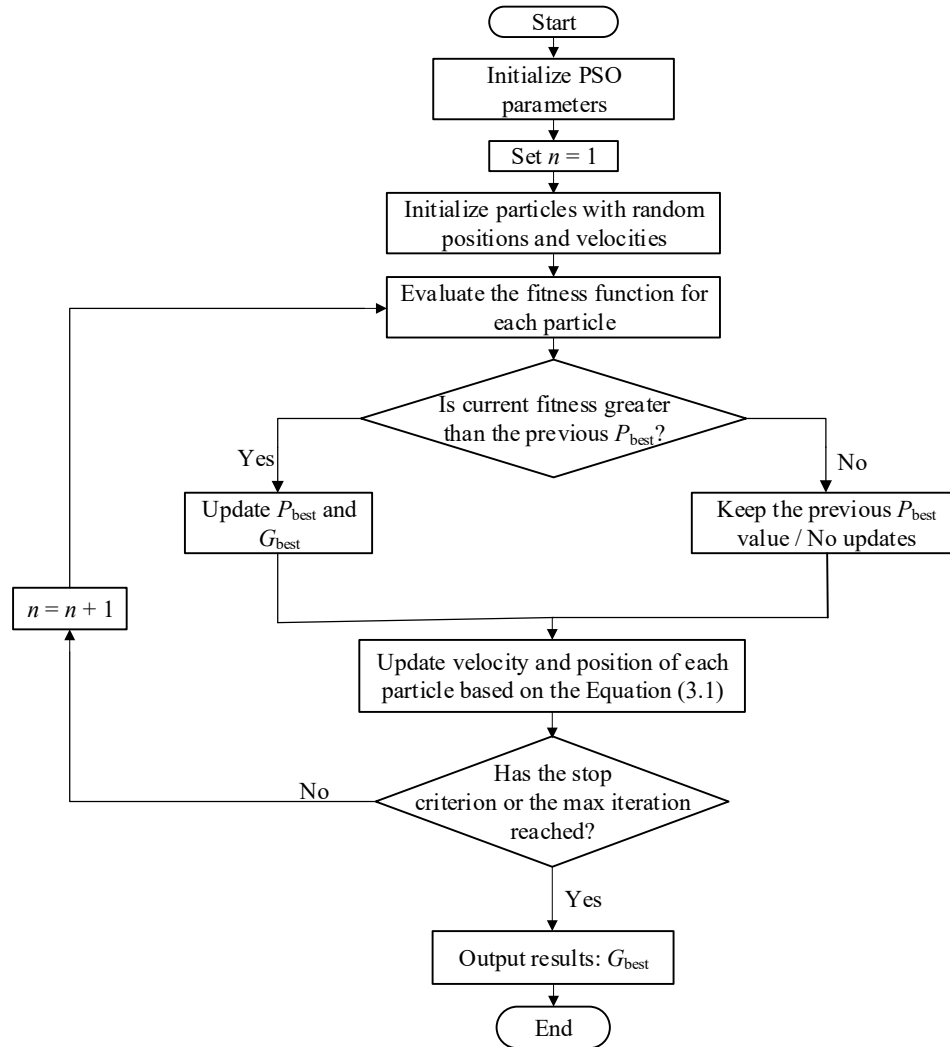
Fig. 3.3. PSO algorithm flowchart.

Eberhart and Shi proposed the parameter constriction coefficient in [14] to guarantee and improve the PSO algorithm's speed of convergence and provide a balance between exploration and exploitation. Moreover, the constriction factors were mathematically established based on the eigenvalue analysis explained in [15] to ensure stable and fast

convergence of the search procedure. Table 3.2 presents the parameters selection for several PSO variants.

TABLE 3.2
PARAMETER SELECTION OF PSO VARIANTS

PSO Variant	Inertia Weight	Acceleration Coefficients
SPSO	Constant, typically in [0.4, 0.9]	Two constants, typically in [0,4]
DWPSO	$\omega_{new} = \omega_s - (\omega_s - \omega_e) \times \dfrac{n}{n_t}$ $\omega_s = 0.4$, $\omega_e = 0.9$	Two constants, typically in [0,4]
TVPSO	Constant, typically in [0.4, 0.9]	$c_1(n) = c_{1s} - (c_{1s} - c_{1e}) \times \dfrac{n}{n_t}$ $c_2(n) = c_{2s} - (c_{2s} - c_{2e}) \times \dfrac{n}{n_t}$ $c_{1s} = 1.5$, $c_{1e} = 2.5$, $c_{2s} = 3$, $c_{2e} = 4$
CCPSO	$\omega = \chi = 0.7298$ $\chi = \dfrac{2}{\left| 2 - \varphi - \sqrt{\varphi^2 - 4\varphi} \right|}$	$c_1 = \varphi_1\chi$, $c_2 = \varphi_2\chi = 1.4962$ $\varphi = \varphi_1 + \varphi_2$ $\varphi > 4, \varphi_1 = \varphi_2 = 2.05$
APSO/ IPSO	$\omega(t) = \omega_{max} - \dfrac{((\omega_{max} - \omega_{min}) \times n)}{n_t}$	$\varphi = 1 - \sigma\dfrac{n}{n_t},\ \ \sigma \in [0,1]$ c_1 multiplied by φ and c_2 multiplied by $(1-\varphi)$; $c_1, c_2 \in [0,4]$

3.2.2. Genetic Algorithm: Strategy and Flowchart

GA is a metaheuristic algorithm inspired by the process of natural selection, which is part of a larger class of evolutionary algorithms (EAs). A simple or standard Genetic Algorithm (SGA) uses three main genetic operators–sequence selection, crossover, and mutation–to search for a globally optimal solution. SGA operates on a population of coded parameter sets called "chromosomes," which are composed of binary strings (or genes) of a specific length that contain information for the corresponding parameter. Each gene has a certain length and contains information regarding the corresponding parameters. The flowchart of GA is presented in Fig. 3.4.
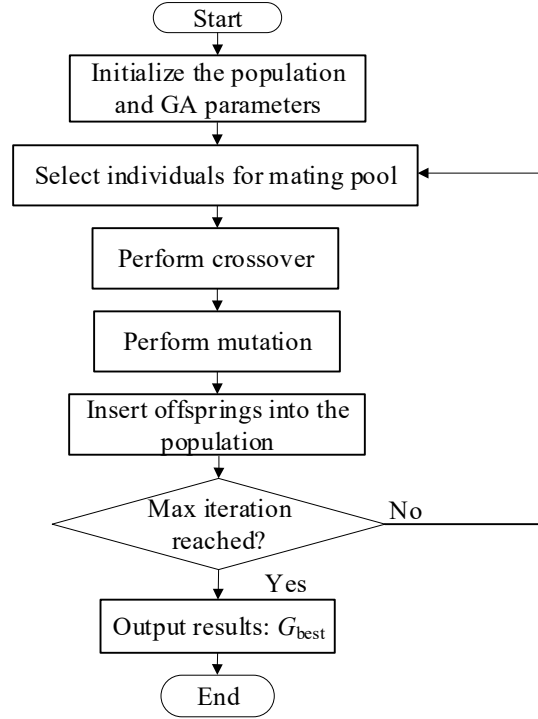
Fig. 3.4. GA flowchart.

3.3. CCPSO-Based Multiparameter Estimation Scheme: Methodology and Flowchart

The constriction factor (χ), as defined in (3.2), is used to tune the PSO parameters, including the inertia weight and acceleration coefficients, to prevent premature and slow convergence. The convergence behavior of the system can be controlled by φ and must be greater than four to guarantee convergence and stability. The equations used are as follows [14]:

$$\chi = \frac{2}{\left| 2 - \varphi - \sqrt{\varphi^2 - 4\varphi} \right|} \tag{3.2}$$

$$\left. \begin{array}{l} \varphi = \varphi_1 + \varphi_2 \\ \varphi > 4, \varphi_1 = \varphi_2 = 2.05 \end{array} \right\} \tag{3.3}$$

$$\left. \begin{array}{l} \omega = \chi = 0.7298 \\ c_1 = \varphi_1 \chi = 1.4962 \\ c_2 = \varphi_2 \chi = 1.4962 \end{array} \right\} \tag{3.4}$$

41

Compared to other PSO-based parameter estimation techniques, in this study, the PMSM's steady-state equations are first decoupled into four speed-independent variables, namely X_1, X_2, Y_1, and Y_2. Subsequently, the PMSM's electrical parameters are separately estimated by proposing three distinct objective functions using the decoupled variables. The strategy for parameter estimation is as follows [16]:

1. Estimate four defined speed-independent variables, i.e., X_1, X_2, Y_1, and Y_2, from the collected experimental data at various speeds and loads using the LS algorithm.
2. Implement CCPSO algorithm with three objective functions, in which the first one (OF_1) is used to estimate R_s and V_{dead} from X_1 and X_2. The second objective function (OF_2) is defined to estimate L_q using Y_1 and the third objective function (OF_3) is developed to estimate L_d and λ_{PM} from Y_2.

The CCPSO algorithm aims to determine the global minimum of objective functions. To guarantee convergence and obtain an accurate estimation, the population size and the number of iterations were set to 50 and 2000, respectively.

Numerous measurements were collected from the experiments, which are explained in detail in Section 3.4. Voltage measurements from V_d and V_q are collected for $M \times N$ various sets of currents $(I_{d,m}, I_{q,n})$, $m = 1, 2, \ldots, M$, and $n = 1, 2, \ldots, N$, at several speeds $\omega_{e,k}$, $k = 1$, $2, \ldots, K$. X_1, X_2, Y_1, and Y_2, as expressed in (3.6), can be estimated using the LS algorithm defined in (3.7) and (3.8).

$$\left. \begin{aligned} V_d &= X_1 - \omega_e Y_1 \\ V_q &= X_2 + \omega_e Y_2 \end{aligned} \right\} \tag{3.5}$$

$$\left. \begin{aligned} X_1 &= R_s I_d + D_D V_{dead} \\ X_2 &= R_s I_q + D_Q V_{dead} \\ Y_1 &= L_{q0} I_q + \beta_1 I_d I_q + \beta_2 I_q^2 + \beta_3 I_d^2 I_q + \beta_4 I_q^3 + \beta_5 I_d I_q^2 \\ Y_2 &= L_{d0} I_d + \alpha_1 I_d^2 + \alpha_2 I_q I_d + \alpha_3 I_d^3 + \alpha_4 I_q^2 I_d + \alpha_5 I_d^2 I_q + \lambda_{PM} \end{aligned} \right\} \tag{3.6}$$

$$X_{LS} = \left(H^T H \right)^{-1} H^T Y \tag{3.7}$$

$$X_{LS} = \begin{bmatrix} X_{1,m,n} \\ X_{2,m,n} \\ Y_{1,m,n} \\ Y_{2,m,n} \end{bmatrix}, H = \begin{bmatrix} 1 & 0 & -\omega_{e,1} & 0 \\ 0 & 1 & 0 & \omega_{e,1} \\ \vdots & \vdots & & \vdots & \vdots \\ 1 & 0 & -\omega_{e,K} & 0 \\ 0 & 1 & 0 & \omega_{e,K} \end{bmatrix}, Y = \begin{bmatrix} V_{d,m,n,1} \\ V_{q,m,n,1} \\ \vdots \\ V_{d,M,N,K} \\ V_{q,M,N,K} \end{bmatrix} \tag{3.8}$$

From (2.27), by incorporating the magnetic saturation and VSI nonlinearity in the PMSM steady-state equations, 15 parameters must be estimated. Three distinct objective functions, as defined in (3.9) are developed to identify the electrical parameters of the PMSM by using the CCPSO algorithm. This can reduce the cross-coupling effects between the parameters and improve estimation accuracy [16].

$$\left.\begin{aligned}
OF_1\left(\hat{R}_s, \hat{V}_{dead}\right) &= \frac{1}{2} \sum_{m,n=1}^{M,N} \left[\left(X_{1,m,n} - \hat{X}_{1,m,n}\right)^2 + \left(X_{2,m,n} - \hat{X}_{2,m,n}\right)^2 \right] \\
OF_2\left(\hat{L}_q\right) &= \frac{1}{2} \sum_{m,n=1}^{M,N} \left[\left(Y_{1,m,n} - \hat{Y}_{1,m,n}\right)^2 \right] \\
OF_3\left(\hat{L}_d, \hat{\lambda}_{PM}\right) &= \frac{1}{2} \sum_{m,n=1}^{M,N} \left[\left(Y_{2,m,n} - \hat{Y}_{2,m,n}\right)^2 \right]
\end{aligned}\right\} \tag{3.9}$$

$\hat{R}_s, \hat{V}_{dead}, \hat{L}_q, \hat{L}_d, \hat{\lambda}_{PM}$ are the estimated parameters, using three defined objective functions. $X_{1,m,n}$ and $X_{2,m,n}$ are obtained from (3.7) and $\hat{X}_{1,m,n}, \hat{X}_{2,m,n}$ are defined as (3.10) which are used in OF_1 to estimate the stator winding resistance and distorted voltage. $M \times N$ are all combinations of dq-axis currents, while $I_{d,m} \in [I_{d,1}, \ldots, I_{d,M}]$, $I_{q,n} \in [I_{q,1}, \ldots, I_{q,N}]$.

$$\left.\begin{aligned}
\hat{X}_{1,m,n} &= \hat{R}_{s,i} I_{d,m} + D_{D,m,n} \hat{V}_{dead,i} \\
\hat{X}_{2,m,n} &= \hat{R}_{s,i} I_{q,n} + D_{Q,m,n} \hat{V}_{dead,i}
\end{aligned}\right\} \tag{3.10}$$

In (3.9), OF_2 is developed to estimate L_q coefficients, i.e., $\hat{L}_{q0}$, $\hat{\beta}_1$, $\hat{\beta}_2$, $\hat{\beta}_3$, $\hat{\beta}_4$, and $\hat{\beta}_5$. $Y_{1,m,n}$ is obtained from (3.7) under various current conditions and $\hat{Y}_{1,m,n}$ can be expressed as follows:

$$\hat{Y}_{1,m,n} = \hat{L}_{q,i} I_{q,n} = \hat{L}_{q0,i} I_{q,n} + \hat{\beta}_{1,i} I_{d,m} I_{q,n} + \hat{\beta}_{2,i} I_{q,n}^2 + \hat{\beta}_{3,i} I_{d,m}^2 I_{q,n} + \hat{\beta}_{4,i} I_{q,n}^3 + \hat{\beta}_{5,i} I_{d,m} I_{q,n}^2 \tag{3.11}$$

The third objective function, denoted as (OF_3), is developed to estimate L_d coefficients, i.e., $\hat{L}_{d0}$, $\hat{\alpha}_1$, $\hat{\alpha}_2$, $\hat{\alpha}_3$, $\hat{\alpha}_4$, and $\hat{\alpha}_5$ and PM flux linkage ($\hat{\lambda}_{PM}$), where $Y_{2,m,n}$ is derived from (3.7) and $\hat{Y}_{2,m,n}$ can be written as:

$$\hat{Y}_{2,m,n} = \hat{L}_{d,i}I_{d,m} + \hat{\lambda}_{PM,i} = \hat{L}_{d0,i}I_{d,m} + \hat{\alpha}_{1,i}I_{d,m}^2 + \hat{\alpha}_{2,i}I_{q,n}I_{d,m} + \hat{\alpha}_{3,i}I_{d,m}^3 + \hat{\alpha}_{4,i}I_{q,n}^2I_{d,m} + \hat{\alpha}_{5,i}I_{d,m}^2I_{q,n} + \hat{\lambda}_{PM,i}$$

(3.12)

Figure 3.5 displays the CCPSO flowchart along with the key implementation steps. Furthermore, variables X_1, X_2, Y_1, and Y_2 are initially estimated using the LS algorithm with the decoupling method (3.8) and then utilized as inputs in the CCPSO algorithm to aid in the evaluation of the objective functions and accurate estimation of the parameters.
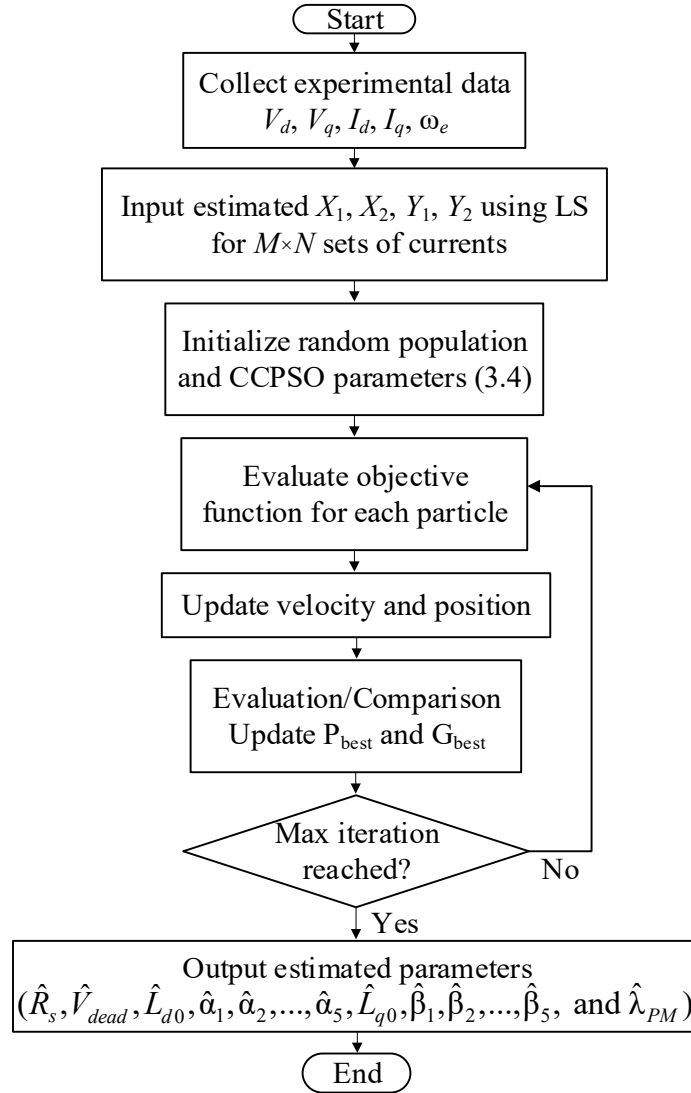
Fig. 3.5. CCPSO-based multiparameter estimation flowchart.

44

3.4. Experimental Investigations

Experimental investigations were conducted on a three-phase laboratory IPMSM, with the design parameters and ratings listed in Table 3.3. The motor under test was a scaled-down prototype for EV applications; the experimental setup is illustrated in Fig. 3.6. The IPMSM was connected to a dynamometer supplied by a multiphase voltage source insulated-gate bipolar transistor (IGBT) inverter. The dyno was controlled using a programmable logic controller (PLC). The IPMSM was controlled by a field-programmable gate array (FPGA) real-time simulator (RTS) called Opal-RT. An inductance, capacitance, and resistance (LCR) meter and a temperature recorder were used to track the parameters and stator winding temperature during the machine operation.

TABLE 3.3
RATINGS AND DESIGN PARAMETERS OF THE STUDIED THREE-PHASE IPMSM

Parameter	Value	Unit	Parameter	Value	Unit
No. of Poles	8		Magnet Type	NdFeB35	
No. of Slots	48		Magnet Flux	0.59	Wb.turns
Rated Speed	575	RPM	Winding Resistance	1.1	Ω
Rated Torque	75	Nm	d-axis Inductance (from FEA)	30.4	mH
Rated Voltage	275	V	q-axis Inductance (from FEA)	87.5	mH
Rated Current	15	A	Switching Frequency	10	kHz
Rated Power	4.25	kW	DC Link Voltage	650	V
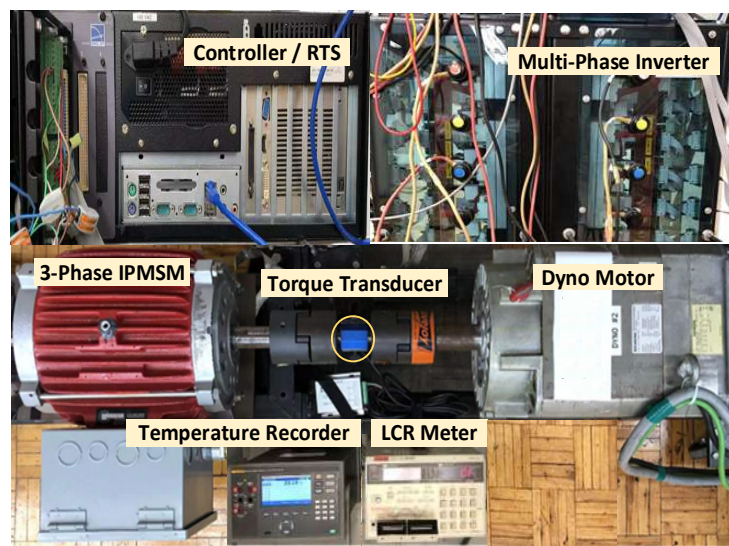
Fig. 3.6. Test rig for experimental validation of proposed methods in this thesis.

FOC was developed for current control, and its implementation is demonstrated by the control block diagram in Fig. 3.7. The proposed estimation approach was developed to estimate the electrical parameters of the IPMSM.

The current sweep test was carried out under various current and speed conditions. The reference d- and q-axis currents were set to 0, -1, -2, ..., -7 A and 4, 5, 6, ..., 13 A, respectively, and measurements were obtained at several motor speeds, including 100, 200, 300, 400, and 500 rpm, as illustrated in Figures 3.8, and 3.9. During the current sweep test, 80 current conditions were applied at five different speeds, yielding 400 different voltage and torque readings. The torque measured from the shaft is shown in Fig. 3.10.
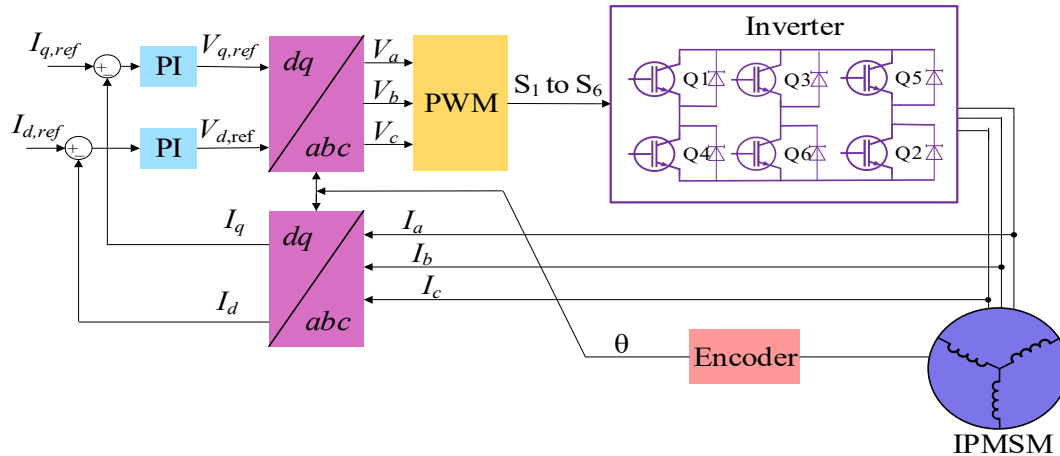
Fig. 3.7. Schematic of current control diagram for the experiment.
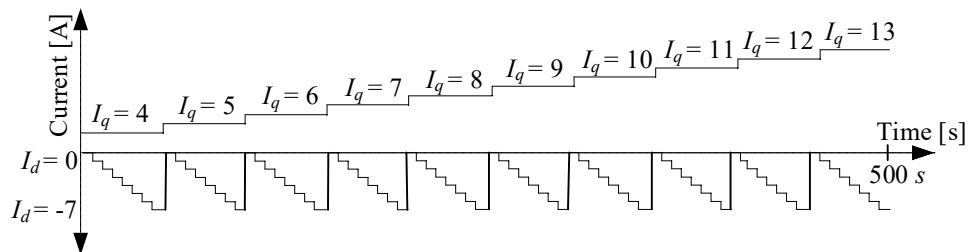
Fig. 3.8. Illustration of current sweep test procedure performed at each speed.

In (2.27), 15 parameters ($R_s, V_{dead}, L_{d0}, \alpha_1, \alpha_2, ..., \alpha_5, L_{q0}, \beta_1, \beta_2, ..., \beta_5$, and λ_{PM}) must be estimated, and because of the rank deficiency of the PMSM equations, it is impossible to estimate them from a single operating point. Therefore, a large amount of data has been collected under various operating conditions to address this issue and accurately estimate all electrical parameters.
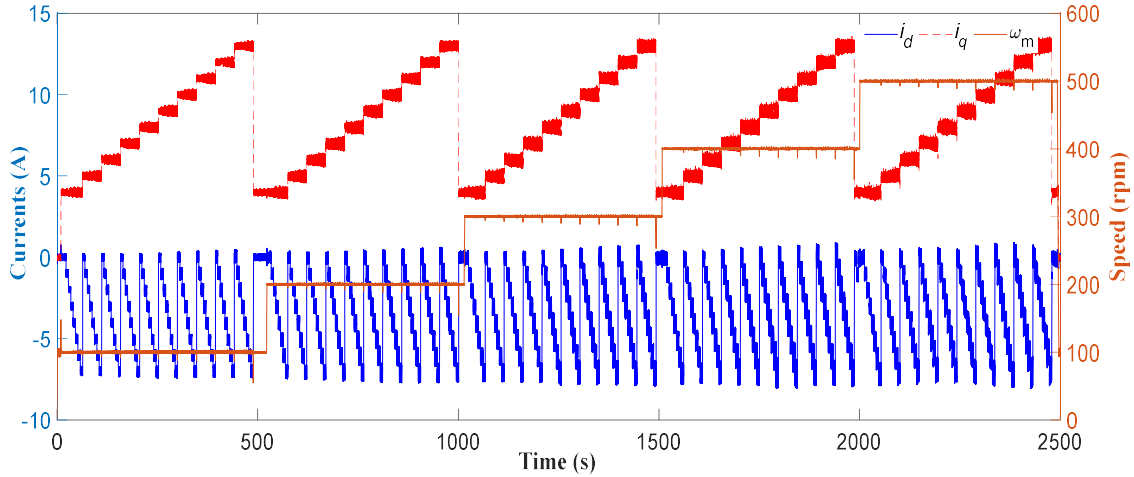
Fig. 3.9. *d*- and *q*-axis current commands in the current sweep test at five different speeds from 100 to 500 rpm.
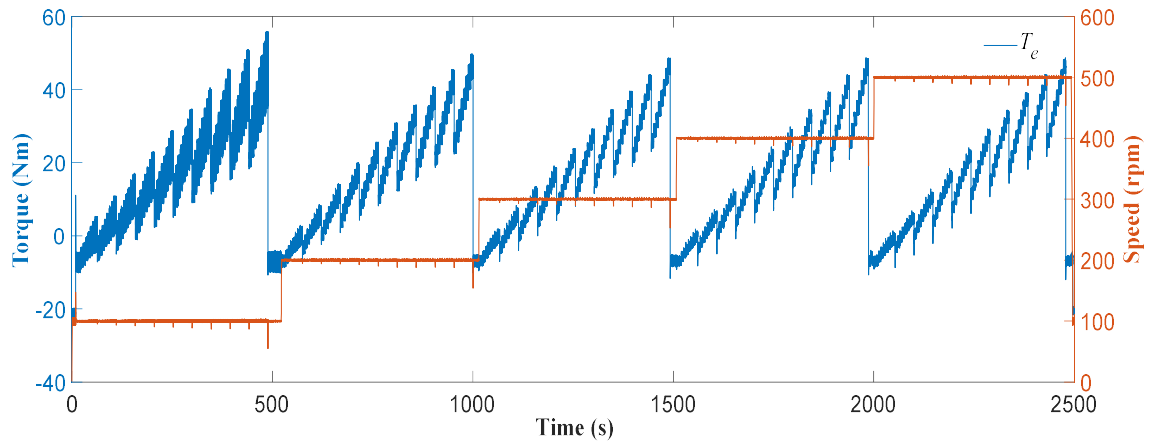
Fig. 3.10. The measured torques from torque transducer in the current sweep test at different speeds.

After the data collection from the experiment, the proposed decoupled parameter estimation method was performed. For each pair of *dq*-axis currents ($I_{d,i}$, $I_{q,i}$), one pair each of X_1, X_2, Y_1, and Y_2 can be estimated from (3.7) using the LS algorithm. Using the estimated speed-independent variables, as shown in Fig. 3.11, under various current conditions, the machine parameters, including the winding resistance, machine inductances, and PM flux linkage, can be accurately estimated by identifying the optimal solutions through function evaluations within the framework of the proposed CCPSO-based parameter estimation method.

VSI nonlinearity has a significant effect on the accuracy of parameter estimation; therefore, its impacts due to dead time were considered, as explained in the previous

47

section, and the average values of distorted coefficients under different current conditions from the experimental data were calculated, as depicted in Fig. 3.12.
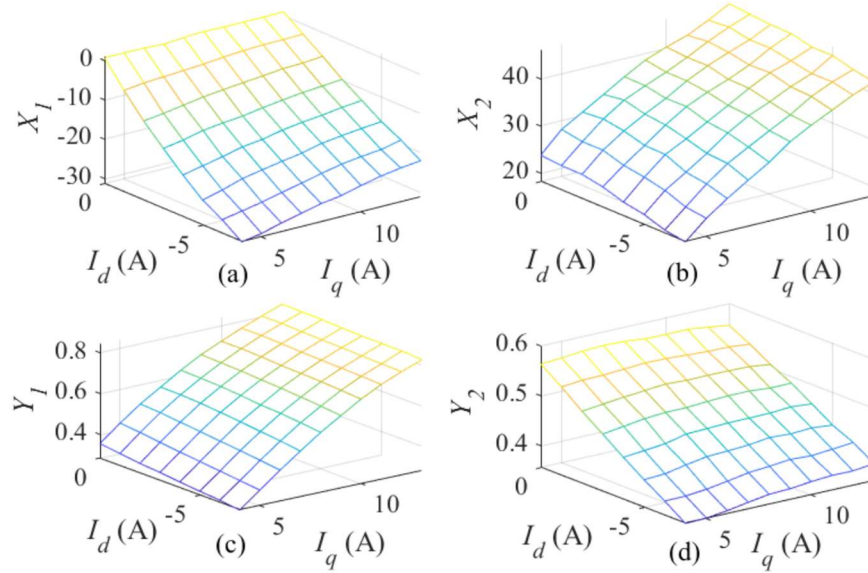
Fig. 3.11. The estimated speed-independent variables under all five speeds: (a) X_1. (b) X_2. (c) Y_1. (d) Y_2.
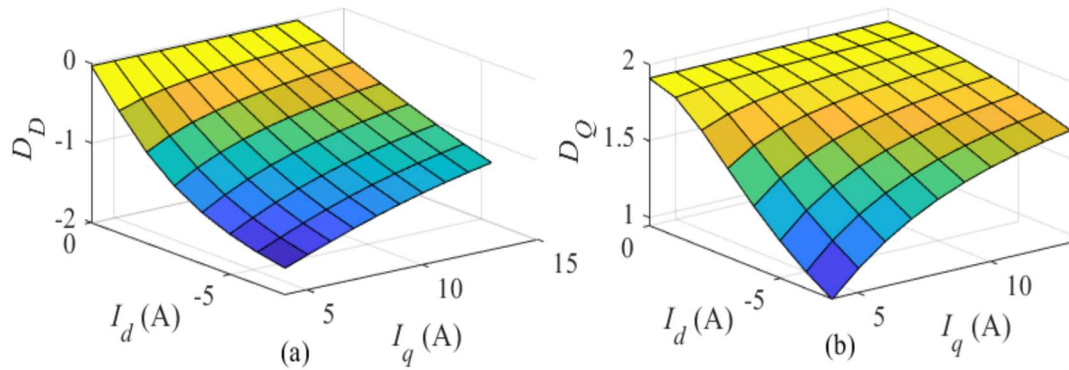
Fig. 3.12. Calculated average of distorted coefficients under different currents: I_d=[0:-7] A, and I_q=[4: 13] A from the current sweep test. (a) D_D. (b) D_Q.

3.5. Multiparameter Estimation Results Analysis

The estimation results for winding resistance and PM flux linkage are presented in Table 3.4. The convergence process of PM flux linkage over the number of iterations is illustrated in Fig. 3.13. The estimation accuracy is evaluated by comparing the estimated resistance with the resistance measured at room temperature using an LCR meter. The estimated R_s includes the VSI's equivalent resistance, stator winding resistance, and connection resistance of the machine circuit. Consequently, it is greater than the winding resistance measured by the LCR. Furthermore, the resistance measurement was performed

when the motor was stationary and at room temperature (20 °C), thereby eliminating any influence of heat that may potentially increase the resistance. It is worth mentioning that the measured resistance is DC resistance. The effects of the time and space harmonics, including the skin and proximity effects, are negligible because of the low frequency of the motor; hence, they were not considered. A temperature recorder was used to monitor the temperature of each phase's windings, from the sensor installed within the windings. The actual winding resistance during machine operation can be calculated using (3.13), where R represents the stator resistance at the recorded temperature, R_{ref} is the resistance at ambient temperature, α is the copper thermal coefficient (0.00393), T is the conductor temperature recorded by the temperature sensors, and T_{ref} is the reference temperature specified at ambient temperature. This method allows for the estimation of the winding resistance at different temperatures using temperature data, and the error can be compensated accordingly.

$$R = R_{ref}(1 + \alpha(T - T_{ref})) \tag{3.13}$$

To validate the accuracy of the estimated PM flux linkage, back EMF tests were performed at speeds of 100, 200, 300, 400, and 500 rpm. The back-EMF phase voltages were obtained at each speed and analyzed using a fast Fourier transform (FFT). The average value obtained from FFT analysis of the no-load back-EMF voltages was found to be 0.565 Wb.turns, and the PM flux linkage estimated using the proposed method was 0.566 Wb.turns. The difference between the estimated and measured PM flux linkages using the proposed CCPSO method is 0.001. Figure 3.14 shows the back-EMF phase voltage waveform at 500 rpm and the fundamental voltage and harmonic components obtained after the FFT analysis.

L_d and L_q vary based on the loading conditions due to magnetic saturation. The proposed method uses polynomial functions to estimate inductances by collecting the dq-axis current and voltage measurements under various loads and speeds.
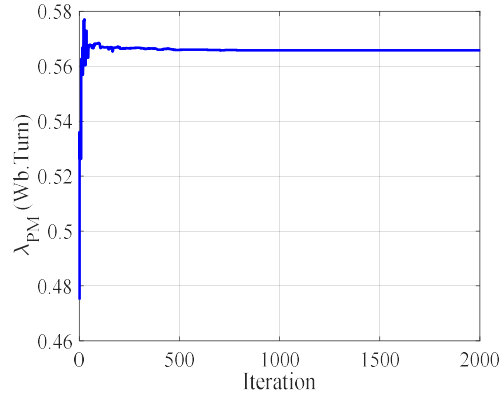
Fig. 3.13. Convergence process of estimated λ_{PM}.

TABLE 3.4
ESTIMATED RESISTANCE AND PM FLUX LINKAGE

Parameters	Measured	Proposed Method
R_s (Ω)	1.1	1.93
λ_{PM} (Wb.turns)	0.565	0.566

(a)

(b)
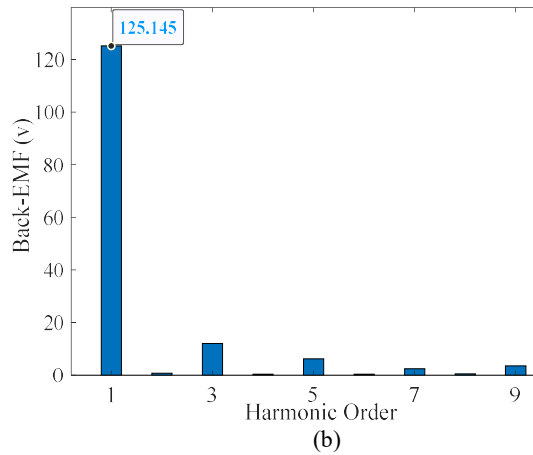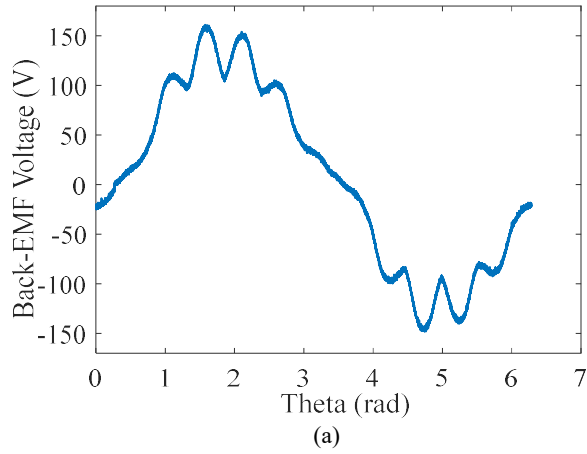
Fig. 3.14. No-load back_EMF test at speed of 500 rpm. (a) Phase voltage waveform. (b) Fundamental and harmonic contents of voltage after FFT.

50

The convergence process of the unsaturated *dq*-axis inductances and saturation coefficients over the number of iterations is illustrated in Fig. 3.15. The estimated L_d and L_q maps are displayed in Fig. 3.16, under the current range of $I_d = [0: -7]$ A, and $I_q = [4:13]$ A.
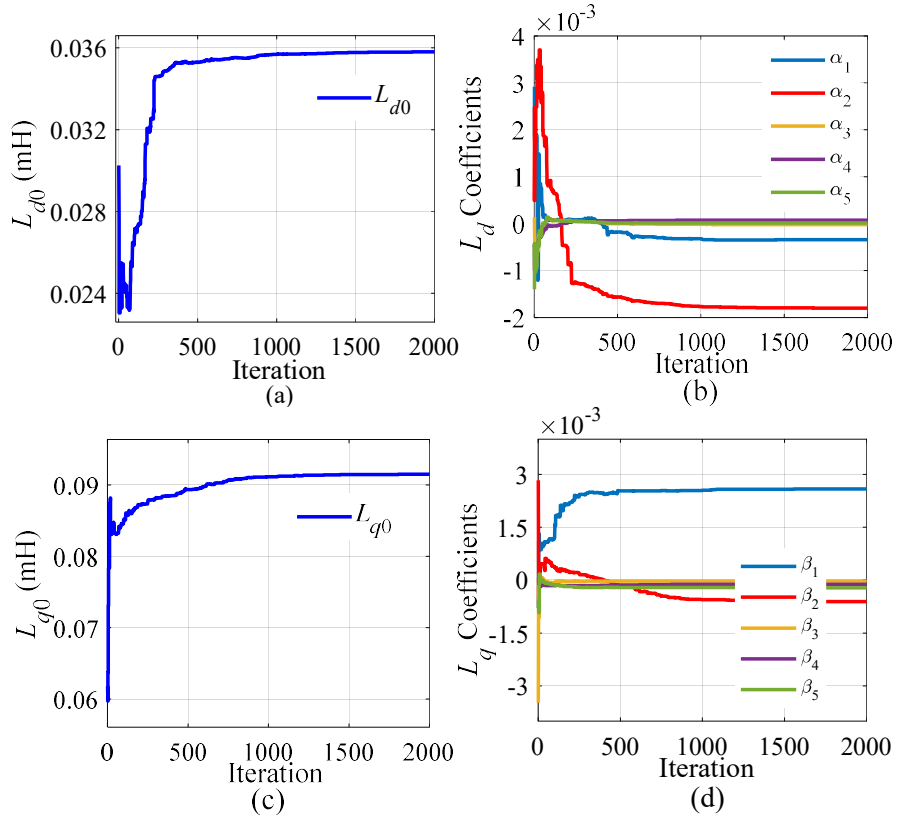
Fig. 3.15. Convergence process of estimated inductance coefficients. (a) L_{d0}. (b) L_d saturation coefficients. (c) L_{q0}. (d) L_q saturation coefficients.
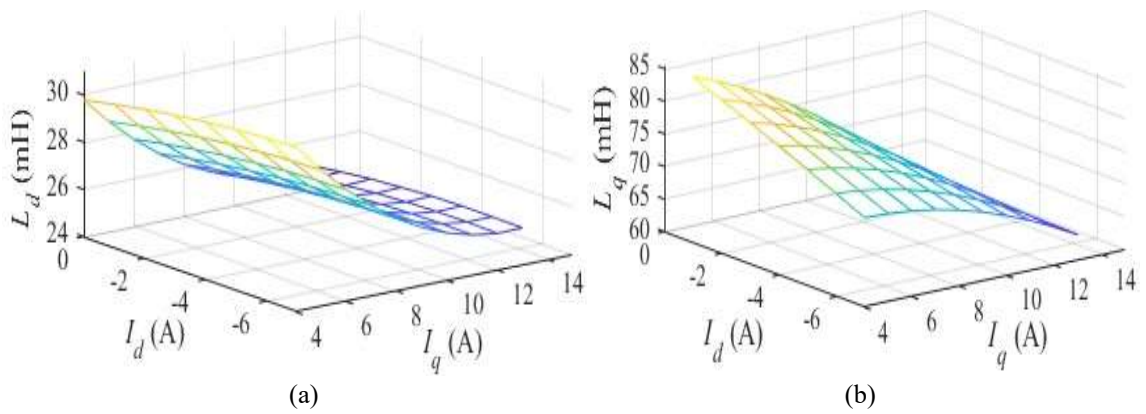
Fig. 3.16. Estimated inductance maps: (a) L_d map. (b) L_q map.

Due to the difficulties in accurately measuring the inductance, the calculated L_d and L_q values under various load conditions were utilized to determine the electromagnetic torques of the machine, which were then compared to the measured torques obtained from a torque transducer. The estimated parameters such as L_d and L_q, as well as the λ_{PM}, were used in the conventional PMSM torque equation to calculate electromagnetic torque. The calculated torque was then compared to the measured torque from the torque transducer, and the resulting maps for the calculated and measured torques, as well as the difference between them, are presented in Fig. 3.17. Because of losses in the machine, such as stray and mechanical losses, the measured shaft torque is generally lower than the calculated electromagnetic torque. The electromagnetic torque results of the proposed CCPSO method have a maximum difference of -1.138 Nm, which represents a maximum error of 4%. The error was evaluated as a percentage using the following equation:

$$Error(\%) = \left| \frac{\tau_{e\_cal} - \tau_{meas}}{\tau_{meas}} \right| \times 100\% \tag{3.14}$$
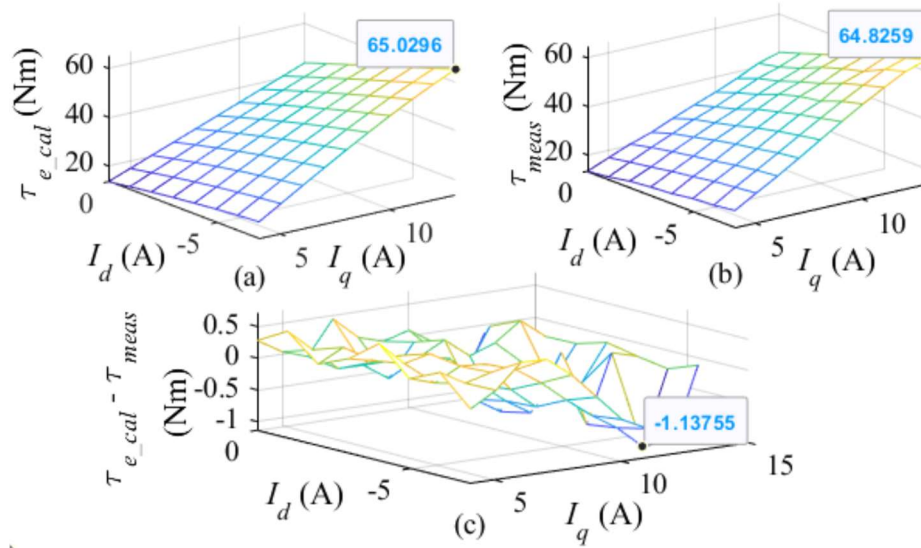
Fig. 3.17. Comparison of torques: (a) Calculated electromagnetic torque. (b) Measured shaft torque. (c) Difference between measured and calculated torques.

3.6. A Comparative Study: Proposed Method vs. Least Squares

To further assess the accuracy of the proposed method, the results of the parameter estimation obtained using the suggested CCPSO method were compared to those obtained

using the LS approach. Table 3.5 presents a comparison of the R_s and λ_{PM} estimation results of the proposed and compared methods. It is evident that the R_s estimated by the proposed CCPSO method is closer to the measured value than that of the LS method. Additionally, the difference between the estimated and measured PM flux linkage from the proposed CCPSO method is 0.001 Wb.turns, which is five times less than the error of 0.005 Wb.turns from the LS approach.

TABLE 3.5
COMPARISON OF ESTIMATED RESISTANCE AND PM FLUX LINKAGE FROM THE PROPOSED AND COMPARED METHODS

Parameters	Measured	Proposed Method	LS Method
R_s (Ω)	1.1	1.93	2.12
λ_{PM} (Wb. turns)	0.565	0.566	0.57

The estimated inductances for the three current conditions are listed in Table 3.6. As can be seen from this table and Fig. 3.18, L_d and L_q vary under different i_d and i_q conditions. The electromagnetic torques calculated using the estimated L_d, L_q, and λ_{PM} from both the CCPSO and LS approaches are provided in Table 3.7 and compared to the actual measured torques.

TABLE 3.6
COMPARISON OF ESTIMATED INDUCTANCES FROM PROPOSED AND COMPARED METHODS

Conditions		CCPSO Method		LS Method	
i_d (A)	i_q (A)	L_d (mH)	L_q (mH)	L_d (mH)	L_q (mH)
0	6	27.67	83.56	27.70	83.57
-2	6	28.15	80.86	28.17	80.87
-2	13	25.34	63.92	25.35	63.91

TABLE 3.7
TORQUE COMPARISON

Conditions		Measured	CCPSO Method	LS Method
i_d (A)	i_q (A)	τ_{meas} (Nm)	τ_{e_cal} (Nm)	τ_{e_cal} (Nm)
0	6	20.45	20.4	20.54
-2	6	24.11	24.16	24.31
-2	13	47.18	47.15	50.51
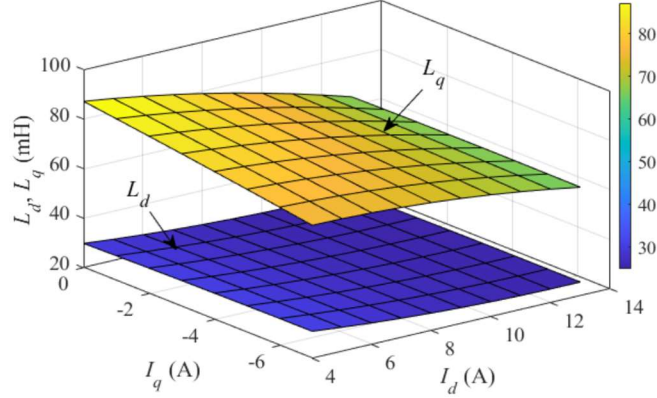
Fig. 3.18. Inductance maps estimated using the compared LS method.

The torques calculated using the proposed CCPSO method are closer to the measured torques than those calculated using the LS method. The maximum error evaluated using (3.13) from the estimated results of the compared LS method is 5.4%, clearly indicating that the parameters estimated using the proposed CCPSO approach are more accurate, with a maximum error of 4%.

3.7. Conclusion

In this chapter, a computationally efficient, noninvasive, and digitally implementable CCPSO approach for PMSM multiparameter estimation is proposed and validated on a three-phase scaled-down 4.25-kW IPMSM. The constriction coefficient is used to tune the PSO parameters and ensure convergence. The IPMSM model was improved by decoupling the parameters into four speed-independent variables and creating three objective functions for the CCPSO algorithm. Experimental investigations were conducted to verify the estimation results of the resistance, PM flux linkage, and dq-axis inductances using the proposed approach.

To illustrate the accuracy of the proposed method in multiparameter estimation, the parameters were compared with the measured values, and comparisons were made with the results obtained through the LS-based estimation. The utilization of the CCPSO algorithm resulted in a higher accuracy of estimated PM flux linkage and resistance, as compared to the LS method. The electromagnetic torque calculated using the estimated dq-axis inductances and PM flux linkage and compared with the measured torques from the torque transducer demonstrated discrepancies of 4.0% and 5.4% from the results of the CCPSO

54

compared to the LS algorithm, indicating an improvement in the multiparameter estimation accuracy achieved through the utilization of the proposed CCPSO algorithm. The effect of winding temperature on the stator winding resistance was considered and compensated using the winding temperature data recorded during the experiment.

3.8. References

[1] Liu, Zhao-Hua, *et al*. "Parameter Estimation for VSI-Fed PMSM Based on a Dynamic PSO with Learning Strategies." *IEEE Transactions on Power Electronics*, vol. 32, no. 4, Apr. 2017, pp. 3154–3165, https://doi.org/10.1109/tpel.2016.2572186.

[2] B. N. Mobarakeh, F. Meibody-Tabar, and F. M. Sargos, "Mechanical sensorless control of PMSM with online estimation of stator resistance," *IEEE Trans. Ind. Appl.*, vol. 40, no. 2, pp. 457–471, Mar./Apr. 2004.

[3] B. Thierry, L. Nicolas, N.M. Babak and M. T. Farid, "Online identification of PMSM parameters: Parameter identifiability and estimator comparative study," *IEEE Trans. Ind. Appl.*, vol. 47, no. 4, pp. 1944–1957, Jul./Aug. 2011.

[4] Y. Zhang, Z. Yin, X. Sun and Y. Zhong, "On-line identification methods of parameters for permanent magnet synchronous motors based on cascade MRAS," *in Proc. 9th Int. Conf. Power Electron. ECCE Asia*, Seoul, Korea, Jun. 2015, pp. 345–353.

[5] Liu, Zhao-Hua, *et al*. "Global Identification of Electrical and Mechanical Parameters in PMSM Drive Based on Dynamic Self-Learning PSO." *IEEE Transactions on Power Electronics*, vol. 33, no. 12, Dec. 2018, pp. 10858–10871, 10.1109/tpel.2018.2801331. Accessed 28 Apr. 2022.

[6] O. Özkaraca. "A Review on Usage of Optimization Methods in Geothermal Power Generation." *Mugla Journal of Science and Technology*, 2018, api.semanticscholar.org/CorpusID:150377782.

[7] Mehta, Sourabh. "Deterministic vs Stochastic Machine Learning." *Analytics India Magazine*, 10 May 2022, analyticsindiamag.com/deterministic-vs-stochastic-machine-learning/.

[8] R. Eberhart and J. Kennedy, "A new optimizer using particle swarm theory," *MHS'95. Proc. Int. Symp. Micro Mach. Hum. Sci.*, 1995, pp. 39-43.

[9] Clerc, Maurice. Particle Swarm Optimization. London; Newport Beach, Calif., Iste, 2010.

[10] Zomaya, Albert Y. Handbook of Nature-Inspired and Innovative Computing: Integrating Classical Models with Emerging Technologies. New York, Springer Science Business Media, 10 Jan. 2006.

[11] Sandre-Hernandez, Omar, et al. "Parameter Identification of PMSMs Using Experimental Measurements and a PSO Algorithm." *IEEE Transactions on Instrumentation and Measurement*, vol. 64, no. 8, Aug. 2015, pp. 2146–2154, 10.1109/tim.2015.2390958. Accessed 28 Apr. 2022.

[12] Engelbrecht, Andries P. *Computational Intelligence*. John Wiley & Sons, 22 Oct. 2007.

[13] A. Ratnaweera, S.K. Halgamuge, and H.C. Watson. "Self-organizing hierarchical particle swarm optimizer with time-varying acceleration coefficients", *IEEE Transaction of Evolutionary Computation*, 8(3):240-255, 2004.

[14] R. C. Eberhart and Y. Shi, "Comparing inertia weights and constriction factors in particle swarm optimization," in *Proc. Cong. Evol. Comput., CEC00 (Cat. No.00TH8512)*, 2000, pp. 84-88, vol. 1.

[15] M. Clerc and J. Kennedy, "The particle swarm - explosion, stability, and convergence in a multidimensional complex space," *IEEE Trans. Evol. Comput.*, vol. 6, no. 1, pp. 58-73, Feb. 2002.

[16] S. Etemadi, H. Cheng, M. S. Toulabi, U. Deshpande and N. C. Kar, "Multiparameter Estimation Accuracy Improvement for PMSMs Using a Constriction Coefficient-Based Particle Swarm Optimization," 2023 *IEEE* 32*nd International Symposium on Industrial Electronics (ISIE)*, Helsinki, Finland, 2023, pp. 1-6, doi: 10.1109/ISIE51358.2023.10227963.

CHAPTER 4

Parameter-Independent Maximum Torque Per Ampere Control for PMSMs

4.1. Introduction

PMSMs can be efficiently controlled in the constant torque region using the MTPA control technique, which maximizes torque production while minimizing the current drawn from the power supply, leading to efficient operation and high performance of the PMSM. Improving the energy efficiency in electric vehicles is significant, and MTPA can achieve this by reducing copper losses and heat generation. The torque in an interior PMSM can be divided into two components: the magnetic torque generated by the permanent magnets, and the reluctance torque resulting from rotor saliency, due to the difference in reluctance between the magnets and iron. The inductance along the d-axis is generally lower than the inductance along the q-axis in an IPMSM. MTPA control uses this reluctance torque to generate more torque at a lower operating speed. The following equations can be used to represent the magnetic and reluctance torques, respectively [1]–[3]:

$$\tau_m = \frac{3}{2} P \lambda_{PM} i_q \tag{4.1}$$

$$\tau_r = \frac{3}{2} P (L_d - L_q) i_d i_q \tag{4.2}$$

For any given torque level, a specific combination of i_d and i_q produces the minimum stator phase current. Multiple combinations of i_d and i_q can produce the same torque, but only one minimizes the stator phase current. The output torque is determined by the current vector with an optimal current angle that minimizes copper losses during machine operation.

Several studies have investigated the use of MTPA control in PMSMs, but there are challenges associated with these methods, such as the need for accurate machine parameters or the development of complex control laws. Furthermore, as the PMSM parameters vary under different operating conditions, failing to account for nonlinearities,

such as magnetic saturation, VSI nonlinearity, cross-coupling, and temperature effects, can result in an MTPA trajectory that fails to minimize the stator current vector or achieve the optimal current angle. To address these challenges, the method outlined in this chapter for MTPA-based control of PMSMs is independent of parameters, considers magnetic saturation, VSI nonlinearity, and temperature effects, and is computationally efficient.

4.2. MTPA Control Strategy

As depicted in the steady-state vector diagram of an IPMSM in Fig. 4.1, the dq-axis currents can be expressed as follows, where I_s is the current vector, and γ is the current angle.

$$\left.\begin{array}{l} I_d = -I_s \sin(\gamma) \\ I_q = I_s \cos(\gamma) \end{array}\right\} \tag{4.3}$$

Substituting (4.3) into (2.6) yields (4.4):

$$\tau_e = \frac{3}{2} P \left\{ I_s \cos(\gamma)\lambda_{PM} - 0.5(L_d - L_q)I_s^2 \sin(2\gamma) \right\} \tag{4.4}$$
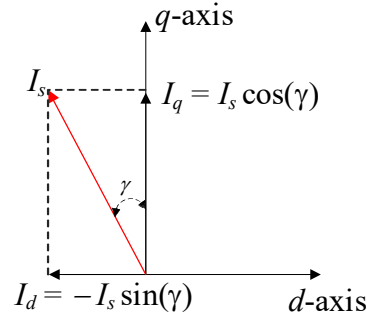
Fig. 4.1. IPMSM steady state vector diagram.

The primary objective of MTPA control is to optimize the torque output for a specific current level while minimizing the magnitude of the stator current, as outlined in (4.5). This implies maximizing τ_e/I_s and setting the differentiation to zero to find the optimal MTPA current angle, as derived in (4.6) and (4.7), respectively. The optimum current angle is denoted by γ_{MTPA}, which can be calculated using (4.8) [4]–[7]. IPMSM characteristics under MTPA control are shown in Fig. 4.2.

$$\left.\begin{array}{l} \max(\tau_e / I_s), \text{ subject to } \dfrac{d(\tau_e / I_s)}{d\gamma} = 0 \\[2mm] \min |I_s| = \sqrt{i_d{}^2 + i_q{}^2} \end{array}\right\} \qquad (4.5)$$

$$\frac{\tau_e}{I_s} = \frac{3}{2} P\left\{ \cos(\gamma)\lambda_{PM} - 0.5(L_d - L_q)I_s \sin(2\gamma) \right\} \qquad (4.6)$$

$$\frac{d(\tau_e / I_s)}{d\gamma} = \frac{3}{2} P\left\{ -\sin(\gamma)\lambda_{PM} - (L_d - L_q)I_s \cos(2\gamma) \right\} = 0 \qquad (4.7)$$

$$\gamma_{\text{MTPA}} = \sin^{-1}\left\{ \frac{\lambda_{PM}}{4(L_d - L_q)I_s} + \sqrt{\frac{\lambda_{PM}^2}{16(L_d - L_q)^2 I_s^2} + \frac{1}{2}} \right\} \qquad (4.8)$$
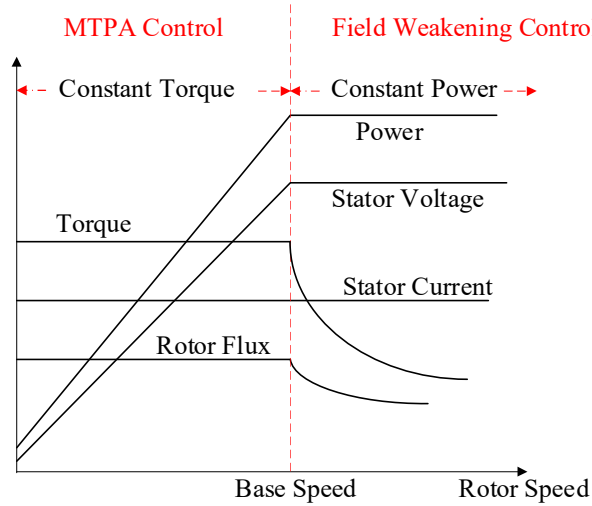
Fig. 4.2. IPMSM characteristics under MTPA control.

4.3. PMSM Parameter-Independent MTPA Control

From (4.8), it can be seen that the optimal current angle depends on *dq*-axis inductances and the PM flux linkage, however, these parameters can vary under different operating conditions. The inductances undergo changes due to magnetic saturation, and the PM flux linkage is influenced by temperature. Furthermore, any discrepancies in the inductance values and PM flux linkage can lead to an inaccurate calculation of the optimal current angle. To address these issues and eliminate the need for online parameter estimation, a parameter-independent model that considers nonlinearities is proposed.

Multiplying i_d and i_q in the steady-state voltage equations yields (4.9), and the summation of the two voltage equations in the *dq*-axis results in (4.10), and the electromagnetic torque equation is derived in (4.12).

$$\left.\begin{array}{l} v_d i_d = R_s i_d^2 - \omega_e L_q i_d i_q + D_D V_{dead} i_d \\ v_q i_q = R_s i_q^2 + \omega_e L_d i_d i_q + \omega_e \lambda_{PM} i_q + D_Q V_{dead} i_q \end{array}\right\} \tag{4.9}$$

$$v_d i_d + v_q i_q = R_s (i_d^2 + i_q^2) + \omega_e \{(L_d - L_q) i_d i_q + \lambda_{PM} i_q\} + V_{dead} (D_D i_d + D_Q i_q) \tag{4.10}$$

$$(v_d - D_D V_{dead}) i_d + (v_q - D_Q V_{dead}) i_q = R_s (i_d^2 + i_q^2) + \omega_e \frac{\tau_e}{1.5P} \tag{4.11}$$

$$\tau_e = \frac{1.5P}{\omega_e}\{(v_d - D_D V_{dead}) i_d + (v_q - D_Q V_{dead}) i_q\} - \frac{1.5P}{\omega_e}\{R_s (i_d^2 + i_q^2)\} \tag{4.12}$$

According to (4.9), the voltage equations are adjusted by the distorted voltage terms resulting from VSI nonlinearity. The model considers the VSI nonlinearity effects since it is often difficult to obtain accurate voltage values due to the absence of voltage sensors, and the output voltages from PI controllers are commonly used. The torque equation, as stated in (4.12), only incorporates the *dq*-axis voltage and current values and is not affected by inductances or the PM flux linkage.

By substituting (4.3) into (4.12), the following torque-per-ampere model and optimal γ_{MTPA} can be obtained.

$$\tau_e = \frac{1.5P}{\omega_e}\{(v_q - D_Q V_{dead}) I_s \cos(\gamma) - (v_d - D_D V_{dead}) I_s \sin(\gamma)\} - \frac{1.5P}{\omega_e} R_s I_s^2 \tag{4.13}$$

$$T = \frac{\tau_e}{I_s}, \quad \frac{d(T)}{d\gamma} = \frac{1.5P}{\omega_e}\{-(v_d - D_D V_{dead}) \cos(\gamma) - (v_q - D_Q V_{dead}) \sin(\gamma)\} = 0 \tag{4.14}$$

$$\gamma_{MTPA} = \tan^{-1}\left\{\frac{-(v_d - D_D V_{dead})}{(v_q - D_Q V_{dead})}\right\} \tag{4.15}$$

The proposed formula for the optimum current angle of the MTPA is not influenced by the parameters of the PMSM and only depends on the *dq*-axis voltages and distorted voltage coefficients resulting from the dead-time effect, as demonstrated in (4.15).

4.4. Gradient Descent Algorithm-Based MTPA Control

To find the optimal MTPA current angle (γ_{MTPA}) at any specific current vector (I_s), a gradient descent algorithm-based angle search method is implemented according to [8], [9] which can be denoted as:

$$\gamma_{t+1} = \gamma_t + \text{sign}(\gamma_t - \gamma_{t-1}) \times \alpha \frac{\partial T}{\partial \gamma} \tag{4.16}$$

To achieve the differential expression, the command voltages can be represented in their discrete form, as they are a function of the current angle γ. The subscript 't' indicates the time instance.

$$\frac{\partial T}{\partial \gamma} = \frac{T_t - T_{t-1}}{\gamma_t - \gamma_{t-1}} \tag{4.17}$$

By substituting (4.17) into (4.16), (4.18) is obtained.

$$\gamma_{t+1} = \gamma_t + \text{sign}(\gamma_t - \gamma_{t-1}) \times \alpha \left(\frac{T_t - T_{t-1}}{\gamma_t - \gamma_{t-1}} \right) \tag{4.18}$$

Where α is the weight that controls the convergence speed, and the optimal current angle calculated at time $t+1$ depends on α and the derivative term. To prevent further updates to the current angle, a small positive threshold was utilized to determine whether the current angle converged toward the MTPA angle.

$$\left| \gamma_{t+1} - \gamma_t \right| < \delta \tag{4.19}$$

Algorithm 1 summarizes the search procedure for determining the optimal angle for maximum torque per ampere in the control. To demonstrate the effectiveness of the proposed MTPA current angle search algorithm, simulation investigations were carried out, and the results are presented in the subsequent section.

Algorithm 1 Gradient Descent Algorithm-Based MTPA Current Angle Search

---

1. Initialize α and set $t = 1$;
2. Calculate τ_e using (4.13);
3. Calculate new current angle using (4.18);

---

4. Check the stop criterion (4.19), if satisfied output optimal $\gamma_{\text{MTPA}} = \gamma_{\text{t}}$;

   Else set $t = t + 1$ and go to step 2.

4.5. Simulation Investigations

The proposed method utilizes only the measured voltages and currents to detect the optimal current angle using a gradient descent algorithm. Figure 4.3 illustrates the control schematic of the proposed current angle search algorithm within the field-oriented control. Simulations are conducted using MATLAB/Simulink.
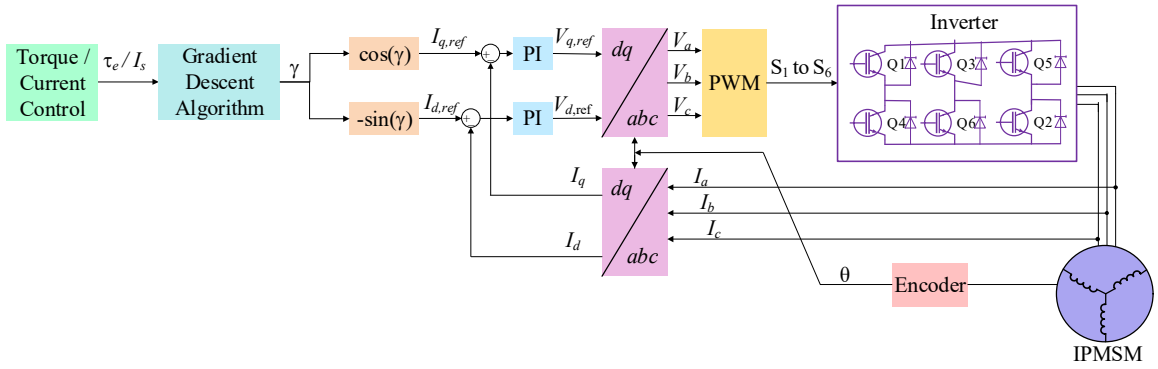

Fig. 4.3. Control block diagram of the proposed gradient descent-based MTPA current angle search strategy.

Gamma was incrementally swept from 1° to 90° in steps of 0.2° during the simulation investigations. At each iteration, the angle was updated using (4.18), and the process was repeated to determine the optimal angle for each torque condition and to generate the minimum commanded current. In the simulation, the speed was fixed at 300 rpm and the load torque was swept at four different torque steps. The initial load torque was set to 10 Nm, and at 2 s, it suddenly increased to 25 Nm. At 4 s, the load torque increased to 40 Nm, and after 2 s, it swept to 65 Nm. As shown in Fig. 4.4 (c), the detected optimal current angles converged to 4.99°, 11.70°, 17.09°, and 23.39° under different torque conditions.

At a load torque of 10 Nm, the optimal current angle was found to converge towards 4.99° while the stator current was held at 2.85 A. As the torque command then changed to 25 Nm, the new current angle was updated through (4.18) and reached the optimal value of 11.70° more quickly, as it initiated the search process from the previous angle.

Figure 4.4 illustrates the simulation results showing the load torque, electromagnetic torque, stator current, *dq*-axis currents, three-phase balanced *abc*-axis currents, and optimal current angle obtained using the proposed angle search algorithm. The simulation validation results were derived from the equations of the three-phase IPMSM model to demonstrate the effectiveness of the proposed method. However, these results are based on analytical equations and do not take into account magnetic saturation and temperature effects.
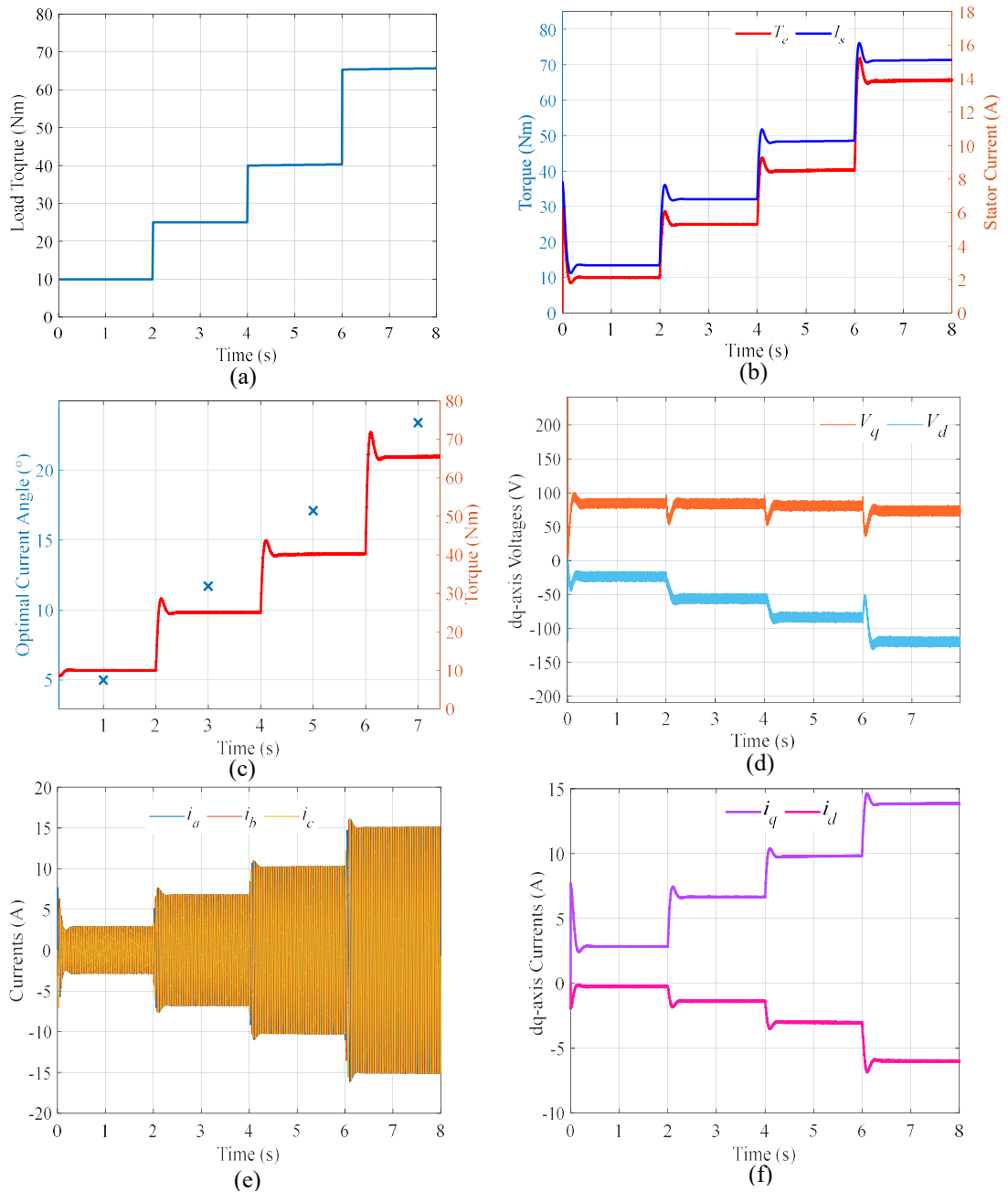
Fig. 4.4. Simulation results for torque sweeping and finding the optimal MTPA current angle based on the proposed angle search algorithm. (a) Commanded load torques. (b) Electromagnetic torques and minimum stator currents during torque sweep. (c) Calculated optimal current angle during torque variation using the proposed method. (d) *dq*-axis voltages. (e) Three-phase *abc*-axis current. (f) *dq*-axis currents generated based on the optimal current angle.

4.6. Conclusion

The MTPA control technique is an effective method for controlling PMSMs, as it maximizes the torque output while minimizing the current, resulting in efficient operation and minimized losses. In this chapter, a method for finding the optimal MTPA current angle based on the gradient descent algorithm is proposed, which can efficiently search for the optimal angle with high accuracy and low computational cost without the need for accurate motor parameters or lookup tables. The proposed angle-search algorithm is parameter-independent and is not influenced by magnetic saturation and temperature effects because it does not include inductance and PM flux linkage terms. The simulation validation was carried out to verify the effectiveness of the proposed search angle algorithm in identifying the optimal angle by sweeping the load torque at different levels within the constant torque region under the base speed and demonstrating the tracking and convergence of the current angle towards the optimal angle.

4.7. References

[1] K. Li and Y. Wang, "Maximum Torque Per Ampere (MTPA) Control for IPMSM Drives Based on a Variable-Equivalent-Parameter MTPA Control Law," in *IEEE Transactions on Power Electronics*, vol. 34, no. 7, pp. 7092-7102, July 2019, doi: 10.1109/TPEL.2018.2877740.

[2] Z. Li, D. O'Donnell, W. Li, P. Song, A. Balamurali and N. C. Kar, "A Comprehensive Review of State-of-the-Art Maximum Torque per Ampere Strategies for Permanent Magnet Synchronous Motors," *2020 10th International Electric Drives Production Conference (EDPC)*, Ludwigsburg, Germany, 2020, pp. 1-8, doi: 10.1109/EDPC51184.2020.9388199.

[3] Ahmed, Adeeb. "Maximum Torque per Ampere (MTPA) Control for Permanent Magnet Synchronous Machine Drive System.", 1 Jan. 2013.

[4] T. Sun, M. Koç and J. Wang, "MTPA Control of IPMSM Drives Based on Virtual Signal Injection Considering Machine Parameter Variations," in *IEEE Transactions on Industrial Electronics*, vol. 65, no. 8, pp. 6089-6098, Aug. 2018, doi: 10.1109/TIE.2017.2784409.

[5] X. Chen, J. Wang, B. Sen, P. Lazari and T. Sun, "A High-Fidelity and Computationally Efficient Model for Interior Permanent-Magnet Machines Considering the Magnetic Saturation, Spatial Harmonics, and Iron Loss Effect," in *IEEE Transactions on Industrial Electronics*, vol. 62, no. 7, pp. 4044-4055, July 2015, doi: 10.1109/TIE.2014.2388200.

[6] T. Sun and J. Wang, "Extension of Virtual-Signal-Injection-Based MTPA Control for Interior Permanent-Magnet Synchronous Machine Drives Into the Field-Weakening Region," in *IEEE Transactions on Industrial Electronics*, vol. 62, no. 11, pp. 6809-6817, Nov. 2015, doi: 10.1109/TIE.2015.2438772.

[7] Z. Li and H. Li, "MTPA control of PMSM system considering saturation and cross-coupling," *2012 15th International Conference on Electrical Machines and Systems (ICEMS)*, Sapporo, Japan, 2012, pp. 1-5.

[8] Z. Li, G. Feng, C. Lai, W. Li and N. C. Kar, "Machine Parameter-Independent Maximum Torque Per Ampere Control for Dual Three-Phase PMSMs," in *IEEE Transactions on Transportation Electrification*, vol. 5, no. 4, pp. 1430-1440, Dec. 2019, doi: 10.1109/TTE.2019.2953656.

[9] Lai, Chunyan, et al. "PMSM Drive System Efficiency Optimization Using a Modified Gradient Descent Algorithm with Discretized Search Space." *IEEE Transactions on Transportation Electrification*, vol. 6, no. 3, Sept. 2020, pp. 1104–1114.

CHAPTER 5

Design of Experiments Using Taguchi Method, and Parameter Sensitivity Analysis

5.1. Introduction

Design of Experiments (DOE) is a statistical tool that is utilized across various types of systems, product design, development, and optimization. This method was first introduced by British statistician Sir Ronald Fischer in the 1920s [1] for agricultural applications, but it has since been widely utilized across multiple fields of science and engineering. DOE is a methodology for systematically applying statistics to experimentation and is a frequent activity in engineering. Consequently, most engineers and scientists use statistics to analyze their experiments, regardless of their background. The one-factor-at-time (OFAT) strategy is still widely practiced by industries, even though the classical, Shainin, and Taguchi DOE methods are statistically more reliable than OFAT [1]–[3].

Parameter estimation is subject to sensitivity to various factors, which should be investigated in the estimation process to improve accuracy, robustness, and motor performance. By understanding the sources of errors and variations, this analysis enables the development of reliable motor-control systems for practical applications. The estimated parameters have some level of uncertainty due to measurement errors, modeling assumptions, and variations in operating conditions. The primary objective of parameter sensitivity analysis through the DOE is to evaluate the estimated parameters, such as inductances, and winding resistance, based on experimental data. This analysis is critical for determining the reliability of the estimated parameters and their influence on motor performance predictions.

The accuracy of parameter estimation is significantly influenced by the quality of the experimental data collected. Utilizing the Taguchi method, an effective and efficient strategy for designing experiments, can improve the outcomes and enhance the accuracy of parameter estimates. Furthermore, the instrument specifications have been evaluated to

ensure they meet necessary standards. Calibration and verification of sensors have been carried out to ensure the precision of measurements.

In the next section, the Taguchi method for designing experiments using orthogonal arrays is employed to account for various influential factors affecting PMSM parameters and their corresponding variations. Additionally, experimental investigations were conducted in accordance with the designed experiments, and the results were collected to analyze parameters sensitivity.

5.2. Taguchi Method for Design of Experiments

The Taguchi method is a structured method used for designing experiments and enhancing processes. Its primary objective is to improve product quality, minimize variability, and limit the impact of external factors. The Taguchi method deviates from other quality engineering approaches by incorporating unique ideas such as minimizing the quality loss function, maximizing the signal-to-noise ratio, and utilizing orthogonal arrays.

The Taguchi method optimizes system performance by determining the best control factor levels and minimizing noise factors. It reduces process variation through experiments and aims to produce high-quality products at low cost. Dr. Genichi Taguchi developed the Taguchi method to study how parameters affect the mean and variance of a process and used orthogonal arrays for experimental design to arrange parameters and their levels. Unlike the factorial design employed in DOE, the Taguchi method tests pairs of combinations, which enables the reduction of collected data and identifies the most influential factors with minimal experimentation, thereby saving time and resources. The steps involved in Taguchi implementation are as follows [4]:

1. Identify key factors affecting performance.
2. Define the range of values for each parameter.
3. Using orthogonal arrays to efficiently design experiments.
4. Conduct experiments and collect data.
5. Analyze experimental data.
6. Apply statistical methods to calculate average responses, Signal-to-Noise Ratios (SNRs).

7. Perform Analysis of Variance (ANOVA), quantify variability from desired target, select appropriate SNR type.

8. Determine optimal parameter settings, most impactful parameters.

9. Validate and fine-tune results, use quality loss function to minimize quality loss and maximize performance.

Taguchi method and DOE are two powerful tools employed in scientific research and industrial applications to optimize processes and enhance product quality. The Taguchi method focuses on robust design, emphasizing the reduction of variations and performance stability. It is particularly effective for identifying the key factors affecting a process and determining the optimal parameter settings while minimizing experimental runs. In contrast, DOE is a more comprehensive approach that encompasses various statistical techniques for systematically designing experiments, analyzing data, and interpreting results. DOE enables researchers to study the effects of multiple variables simultaneously, thus providing a thorough understanding of complex processes. Taguchi method is efficient for quick optimization with fewer experiments, while DOE offers a more detailed and in-depth analysis of the factors influencing a system.

The parameters of the PMSM, such as the stator winding resistance, dq-axis inductances, and PM flux linkage, are subject to variations under different operating conditions such as load torque, current, speed, and temperature. For instance, an increase in temperature causes an increase in winding resistance and a decrease in PM flux linkage, leading to estimation errors. To enhance estimation accuracy, it is crucial to optimize these control factors. The Taguchi method, utilizing orthogonal arrays, is implemented in order to conduct experiments that account for the effects of torque, speed, and temperature, and to evaluate the influence of diverse levels of these factors on parameter variations through the examination of collected experimental data.

5.3. Methodology and Experimental Investigations

An experimental investigation was carried out on the three-phase IPMSM with the designated parameters outlined in Table 3.3 and the utilized sensors, along with their accuracy and specifications, presented in Table 5.1. Figure 3.6 displays the complete test rig, including the instruments employed during the experimentation. The IPMSM is

coupled with a dynamometer and is powered by an IGBT VSI. An FPGA-based real-time simulator was utilized for motor control. The current, torque, and position sensors were calibrated, and the shaft between the IPMSM and dynamometer was precisely aligned using a laser shaft alignment tool.

TABLE 5.1
SENSORS AND INSTRUMENTS UTILIZED IN EXPERIMENT

Position Sensor	Incremental Encoder
Torque Transducer	100 Nm, Accuracy ≤ 0.1 Nm
Current Transducer	25 A LEM Isolated Current Sensor, Accuracy $\pm 1\%$
Temperature Sensors	Two-wire Platinum Resistance Thermometers (PRTs)
Fluke Infrared Thermal Imager	Thermal Sensitivity $\leq 0.1°C$
Fluke Data Acquisition	Accuracy 0.01 %

In the experiment conducted in this study, three key factors were investigated: temperature, torque, and speed. The temperature was examined at two distinct levels, 28 °C and 55 °C. Torque, a critical variable in the study, was analyzed across three levels: low, medium, and high. At each of these torque levels, four different values were explored for 12 unique combinations within the torque factor. The optimal current angle was identified using the MTPA control-based current angle search method explained in the previous chapter to minimize the stator current at each torque level. Speed, the third factor, was tested at three levels: 50, 250, and 500 rpm. Therefore, this study aimed to understand the impact of these factors at their respective levels on experimental outcomes.

To select the appropriate orthogonal array, an L18 array was chosen based on the specific characteristics of the experimental design, which involved the investigation of three key factors: temperature, torque, and speed, each at varying levels. The reason for selecting the L18 orthogonal array is its capacity to accommodate combinations of levels for these factors. Given that temperature has two levels, torque has three levels, and speed has three levels, the total number of possible combinations is 2 (temperature) × 3 (torque levels) × 3 (speed levels) = 18. The L18 orthogonal array was chosen because it allowed for 18 experimental runs. Although this number is fewer than the total possible combinations, it still enables us to obtain valuable insights into the effects of the factors on

the response variable while maintaining a manageable number of experiments. The experimental design structure, which involved selecting L18 for the orthogonal array, is presented in Table 5.2. The torque range is categorized into three distinct levels, namely 0-10%, 40-50%, and 85-95% of the rated torque, which is 70 Nm, as specified in Table 5.3, and were applied during the experiment.

TABLE 5.2
STRUCTURE OF L18 ORTHOGONAL ARRAY FOR THE EXPERIMENT

Run	Torque (%)	Temperature (°C)	Speed (rpm)
1	0-10 %	28	50
2	40-50 %	28	50
3	85-95 %	28	50
4	0-10 %	28	250
5	40-50 %	28	250
6	85-95 %	28	250
7	0-10 %	28	500
8	40-50 %	28	500
9	85-95 %	28	500
10	0-10 %	55	50
11	40-50 %	55	50
12	85-95 %	55	50
13	0-10 %	55	250
14	40-50 %	55	250
15	85-95 %	55	250
16	0-10 %	55	500
17	40-50 %	55	500
18	85-95 %	55	500

TABLE 5.3
LEVELS OF LOAD TORQUE VARIATIONS

Torque Level	Torque Range (%)	Torque Values (Nm)
Low	0 to 10	0, 3, 5, 7
Medium	40 to 50	28, 30, 32, 35
High	85 to 95	59, 61, 63, 65

5.4. Experimental Results: Parameter Sensitivity Analysis

It is commonly observed that PMSM parameters vary under different machine operating conditions. Considering this, the effects of the load torque, motor speed, and stator winding temperature on PMSM parameters are investigated using the results of the designed experiment executed using the Taguchi method, which was previously described. Figure 5.1 demonstrates various torques during testing, which were applied at three different speeds, resulting in several voltage and current measurements. Figure 5.2 illustrates the dq-axis currents corresponding to each torque generated through MTPA control and applied at different motor speeds.
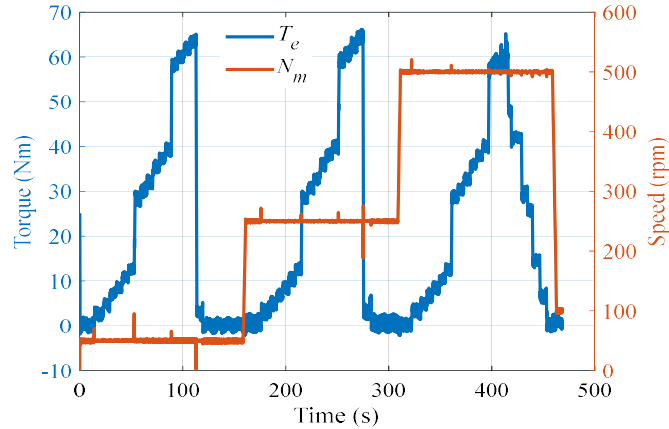
Fig. 5.1. Experimental validation. Three levels of torque: low, medium, and high, at three speed levels: 50, 250, and 500 rpm.
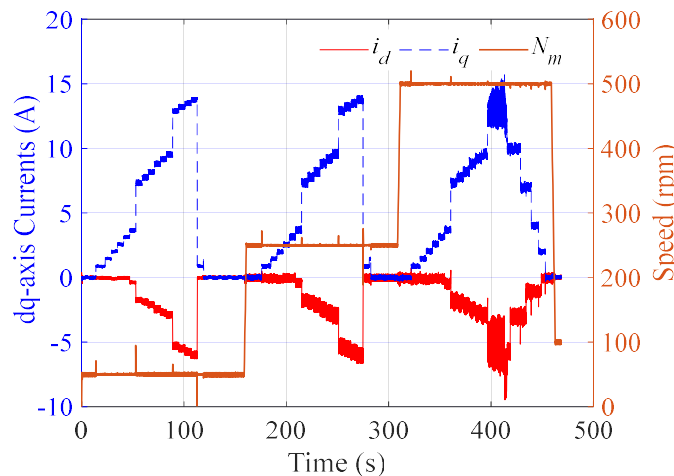
Fig. 5.2. dq-axis current variations at different speed conditions.

71

The accuracy of inductance estimation is highly dependent on the accuracy of resistance estimation. Even minor variations in resistance can result in significant changes in inductance estimates. Therefore, if the resistance is initially estimated, it can significantly enhance the precision of the other parameter estimations [5]. The approach outlined in [6] is utilized for estimating the resistance, expressed in (5.1), which involves utilizing only *dq*-axis voltages and currents without requiring *dq*-axis inductance and PM flux linkage values.

$$
\begin{aligned}
&\omega_{e,j}(V_{d,i}I_{d,i} + V_{q,i}I_{q,i}) - \omega_{e,i}(V_{d,j}I_{d,j} + V_{q,j}I_{q,j}) \\
&= V_{dead}\left[\omega_{e,j}(D_{Q,i}I_{q,i} + D_{D,i}I_{d,i}) - \omega_{e,i}(D_{Q,j}I_{q,j} + D_{D,j}I_{d,j})\right] \\
&+ R_s\left[\omega_{e,j}(I_{d,i}^2 + I_{q,i}^2) - \omega_{e,i}(I_{d,j}^2 + I_{q,j}^2)\right], \quad 1 \le i, j \le K
\end{aligned}
\tag{5.1}
$$

In (5.1), the average measurements of the voltage and current are employed, and *K* sets of steady-state voltage equations for parameter estimation are defined. In the case of the designed experiments at each torque level (low, medium, and high), four torque values were applied to solve the rank deficiency issue and to construct more equations for parameter estimation. D_D and D_Q are the mean values of the distorted coefficients over one electrical cycle calculated using (2.20). In a steady state, VSI distorted voltages are considered constant, and average measurements act as a filter, eliminating measurement noise to enhance the estimation accuracy. From (5.1), the values of R_s and V_{dead} are estimated first and then substituted in the PMSM steady-state voltage equations (2.19) while considering the effects of magnetic saturation and VSI nonlinearity. Magnetic saturation can be modeled using the following linear equation:

$$
\left.
\begin{aligned}
L_d &= L_{d0} + \alpha_1 I_d + \alpha_2 I_q \\
L_q &= L_{q0} + \beta_1 I_q + \beta_2 I_d
\end{aligned}
\right\}
\tag{5.2}
$$

where α_1 and β_1 are self-saturation coefficients, and α_2 and β_2 are the cross-saturation coefficients. Since the cross-saturation effect is generally much smaller than the self-saturation effect, it can be disregarded in this study.

The results of the experimental verifications indicate inconsistencies in the accuracy of the estimated parameters under varying operating conditions. A higher torque results in

higher currents, which contributes to a better signal-to-noise ratio, as higher currents are less affected by noise. As the torque applied increases, the current also increases, resulting in a decrease in the resistance estimation error. The resistance estimation errors for different load torques and speeds are presented in Fig. 5.3.

It can be seen from Fig. 5.3 that an increase in torque resulted in a decrease in the estimation error, and the lowest error occurred at the highest torque level. This is because a higher current flows through the windings, which leads to a more accurate estimation of winding resistance. In addition, the error in the resistance estimation is influenced by speed, and higher speeds can cause more distorted currents, leading to an increased resistance estimation error. Therefore, the lowest resistance estimation error occurred at the highest torque and lowest speed, where the current was higher and less distorted. The winding resistance is also affected by winding temperature, the resistance is higher at higher winding temperatures as shown in Table 5.5, average values for resistance and estimation error are calculated at 28 °C and 55 °C are shown in Table 5.5.
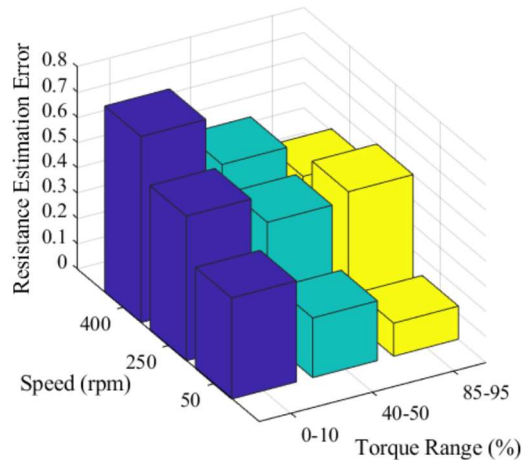
Fig. 5.3. Resistance estimation error under different torque and speed conditions at 28 °C.

TABLE 5.4
RESISTANCE VARIATION WITH WINDING TEMPERATURE

Average Resistance Estimated at 28 °C	1.587 Ω
Average Estimation Error at 28 °C	0.442
Average Resistance Estimated at 55 °C	1.756 Ω
Average Estimation Error at 55 °C	0.596

Figures 5.4 and 5.5 depict the *dq*-axis inductance variations under different torque and speed conditions. The graphs illustrate that the inductances decreased under high-torque conditions, which may be due to the nonlinearity induced by saturation at higher torque levels. The lowest *q*-axis inductance occurred when the IPMSM operated at the highest torque and speed simultaneously. The estimation error of the inductances may be reduced at higher speeds as the inductance terms in the PMSM voltage equation are multiplied by speed, resulting in an inverse proportionality to the rotor speed, which can also be applied to the PM flux linkage [6], [7].
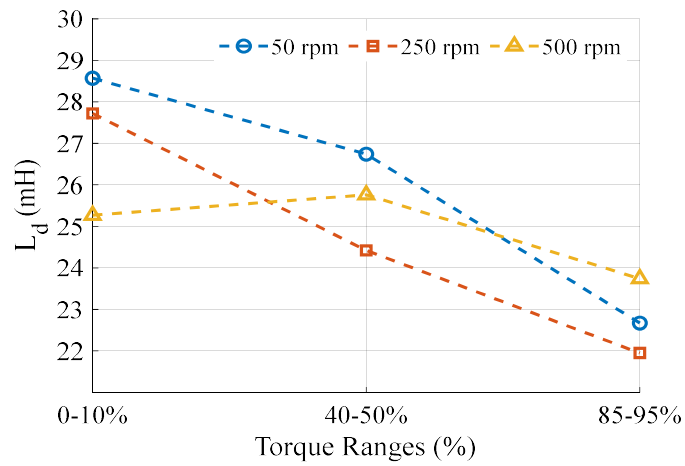
Fig. 5.4. *d*-axis Inductance estimation variation under different torque and speed conditions.
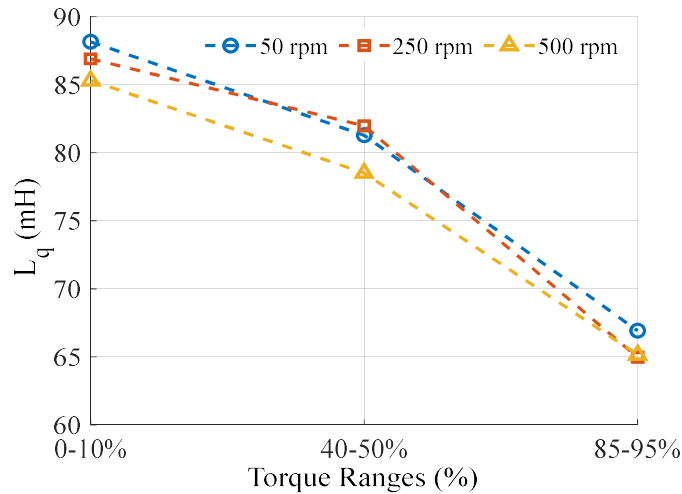
Fig. 5.5. *q*-axis Inductance estimation variation under different torque and speed conditions.

5.5. Conclusion

Under various operating conditions, the PMSM parameters may exhibit variations, and it is essential to understand their behavior and changes. To improve the quality of the experimental data for parameter estimation and sensitivity analysis, the Taguchi method was used for the design of the experiment, which was conducted on a three-phase laboratory IPMSM to validate the estimation results. Three primary factors impacting the parameters were examined under different levels: load torque, speed, and temperature. The data collected from the experimental validation indicated that the winding resistance could be better estimated at higher load torques and lower speeds. Additionally, the inductances were higher at lower torques and demonstrated greater accuracy at higher speeds.

5.6. References

[1] Jankovic, Aleksandar, et al. "Designing the Design of Experiments (DOE) – an Investigation on the Influence of Different Factorial Designs on the Characterization of Complex Systems." *Energy and Buildings*, vol. 250, 1 Nov. 2021, p. 111298.

[2] Gope, Deepayan, and Sandeep Kumar Goel. "Design Optimization of Permanent Magnet Synchronous Motor Using Taguchi Method and Experimental Validation." *International Journal of Emerging Electric Power Systems*, vol. 22, no. 1, 25 Dec. 2020, pp. 9–20, https://doi.org/10.1515/ijeeps-2020-0169.

[3] Ilzarbe, L. et al., Practical Applications of Design of Experiments in the Field of Engineering. A Bibliographical Review. Quality and Reliability Engineering International, 2008. 24(4): pp. 417–428.

[4] Helder Jose Celani. *Robust Design and Taguchi Method Application*. 2013.

[5] J. Long, M. Yang, Y.-Q. Li, Y.-Y. Chen, and D.-G. Xu, "Parameter identification of permanent magnet synchronous motors: Sequence strategy comparative study," in *Transportation Electrification Asia-Pacific (ITEC Asia-Pacific), 2017 IEEE Conference and Exp*, 2017, pp. 1–6.

[6] G. Feng, C. Lai and N. C. Kar, "A Novel Current Injection-Based Online Parameter Estimation Method for PMSMs Considering Magnetic Saturation," in *IEEE Transactions on Magnetics*, vol. 52, no. 7, pp. 1-4, July 2016, Art no. 8106004, doi: 10.1109/TMAG.2016.2525805.

[7] Z. Li, G. Feng, C. Lai, D. Banerjee, W. Li and N. C. Kar, "Investigation of on-Line Parameter Estimation for Interior PMSMs Considering Current Injection and Machine Operating Conditions," *2018 21st International Conference on Electrical Machines and Systems (ICEMS)*, Jeju, Korea (South), 2018, pp. 1395-1400, doi: 10.23919/ICEMS.2018.8549025.

CHAPTER 6

Conclusion and Future Work

6.1. Conclusion

This thesis focuses on the development of noninvasive multiparameter estimation schemes for estimating the parameters of PMSMs in industrial applications, particularly in electric vehicles. The importance of accurate and efficient parameter estimation lies in the design of optimal controllers, fault detection and diagnosis, performance optimization, and condition monitoring. A mathematical model was proposed for a three-phase interior PMSM that accounts for nonlinearities, and the electrical parameters of the PMSM, including the stator winding resistance, PM flux linkage, and *dq*-axis inductances, were accurately estimated. A decoupled scheme was developed to reduce both the cross-coupling effects between the parameters and the computational burden in parameter estimation. The model also considers the effects of magnetic saturation on the *dq*-axis inductances and VSI nonlinearity effects. A Particle Swarm Optimization algorithm was developed based on the constriction coefficient to enhance the efficiency of the estimation process. An experimental validation was conducted on a laboratory-scale 4.25-kW IPMSM, and the results were analyzed to validate the accuracy of the proposed method. The inductance maps, resistance, and PM flux linkage were obtained, error estimation was performed to validate the estimated parameters, and a comparative analysis was conducted to compare the CCPSO-based estimation technique with the LS method, demonstrating the superior accuracy and performance of the proposed method.

PMSMs can be effectively controlled in the constant torque region through the Maximum Torque Per Ampere control technique, which maximizes torque production while minimizing current drawn from the power supply, leading to high levels of performance and efficiency. This control technique involves the calculation of the optimal current angle to minimize copper losses and heat generation during machine operation, particularly in electric vehicles. However, challenges such as the need for accurate machine parameters or the development of complex control laws may arise during implementation. Additionally, failing to account for nonlinearities can result in an MTPA trajectory that

fails to minimize the stator current vector or achieve the optimal current angle. A parameter-independent model has been proposed for MTPA-based control of PMSMs that considers magnetic saturation and temperature effects and is computationally efficient. This model eliminates the need for online parameter estimation and is based on the steady-state voltage equations and the electromagnetic torque equation. The proposed method is validated through simulation investigations and can enhance motor performance and maximize torque production.

The Taguchi method was employed to design the experiments, which utilized orthogonal arrays to enhance the quality and reliability of the testing process while minimizing inconsistencies. Three main factors affecting the parameters, including temperature, load torque, and speed, were incorporated into the Taguchi experimental design, with each factor varying at different levels. This variation enabled a comprehensive examination of the impact of these factors on the variations in the PMSM parameters. The data collected from the experiments were subsequently utilized for sensitivity analysis of the parameters and to gain insights into their sensitivity and behavior under different operating conditions.

6.2. Future Work

Future work will focus on the following aspects:

1. Investigating parameter estimation under field or flux-weakening region operation to achieve optimized performance and control of the motor beyond the rated speed.
2. Incorporating the core loss into parameter estimation, utilizing mathematical models, and experimental validation, as it has a significant impact on the performance of permanent magnets, stator windings, and the magnetic flux distribution, and can lead to improved accuracy in the estimated parameters.
3. Considering temperature effects on PM flux linkage estimation and permanent magnet demagnetization at high temperatures.
4. Development of an artificial intelligence-based neural network technique to enhance the accuracy and efficiency of parameter estimation.

5. Incorporating SNR analysis to assess parameter sensitivity and optimize input factors, along with ANOVA, to enhance the efficiency and reliability of the Taguchi experimental design methodology, thereby improving the quality of experimental results.

APPENDIX

Permission For Using IEEE Publications

VITA AUCTORIS

NAME:	Sana Etemadi
PLACE OF BIRTH:	Vienna, Austria
YEAR OF BIRTH:	1996
EDUCATION:	Adib Farzaneh High School, Tehran, Iran, 2015
	University of Tehran, B.Sc., Tehran, Iran, 2019
	University of Windsor, M.Sc., Windsor, ON, 2023